J. Fluid Mech. (2013), *vol.* 732, *pp.* 537–570. © Cambridge University Press 2013
doi:10.1017/jfm.2013.417

Two-layer shallow-water dam-break solutions for gravity currents in non-rectangular cross-area channels

Marius Ungarish†

Department of Computer Science, Technion, Haifa 32000, Israel

(Received 4 February 2013; revised 2 August 2013; accepted 8 August 2013;
first published online 12 September 2013)

We consider the propagation of a high-Reynolds-number gravity current in a horizontal channel along the horizontal coordinate x. The bottom and top of the channel are at $z = 0, H$, and the cross-section is given by the quite general $-f_1(z) \leqslant y \leqslant f_2(z)$ for $0 \leqslant z \leqslant H$. We develop a two-layer shallow-water (SW) formulation, and we implement it for the solution of the dam-break problem. The dependent variables are the position of the interface, $h(x, t)$, and the velocity (averaged over the area of the current), $u(x, t)$. The non-rectangular cross-section geometry enters the formulation via $f(h)$ and integrals of $f(z)$ and $zf(z)$, where $f(z) = f_1(z) + f_2(z)$ is the width of the channel. For a given geometry $f(z)$, the free input parameters of the lock-release problem are: (i) the height ratio H/h_0 of ambient to lock; and (ii) the density ratio of 'light' to 'heavy' fluids, R. We show that the dam-break problem is amenable to solution by the method of characteristics, but various complications (internal jumps, critical restrictions) appear when the return flow in the ambient is significant; these features are not captured by a one-layer shallow-water model. The role of the non-standard geometry in the detection and calculation of the internal and reflected jumps, and on the dam-break flow field, is elucidated. The methodology is illustrated for Boussinesq flow in typical geometries: power-law ($f(z) = bz^{\alpha}$, where b, α are positive constants), trapezoidal and circle (full or sector); we solved for full-depth ($H = 1$) and part-depth ($H > 1$) lock-release configurations. The approach seems to work well: in all the tested cases, the solution was obtained with simple mathematical and numerical tools (a Runge–Kutta integrator and a secant-method solver); the insights are compatible with our previous understanding of the problem; and the standard (rectangular) case is recovered in the appropriate limit (i.e. when the side-boundaries of the trapezium cross-section are vertical or far apart). A comparison of the speed of propagation with available experiments is also presented, and the agreement is satisfactory. The present solution is a significant generalization of the classical two-layer gravity–current dam-break problem. The classical formulation for a rectangular (or laterally unbounded) channel is now just a particular case, $f(z) =$ const., in the wide domain of cross-sections covered by the new model.

Key words: geophysical and geological flows, gravity currents

† Email address for correspondence: unga@cs.technion.ac.il

https://doi.org/10.1017/jfm.2013.417 Published online by Cambridge University Press

1. Introduction

A gravity current (GC) appears when fluid of one density, ρ_c, spreads into a fluid of another density, ρ_a, and the propagation is, mainly, in the horizontal direction. Gravity currents occur at a variety of scales throughout nature. Examples include oceanic fronts, avalanches, seafloor turbidity currents, pyroclastic flows and lava flows. Most studies have focused on the flow of currents that propagate on the flat bottom (or top) of a rectangular channel. If the Reynolds number (Re) is large (as assumed here), the lateral boundaries of such a container are unimportant (see Simpson 1997; Ungarish 2009). However, GCs generated and spreading in channels with non-rectangular cross-sections are realistic configurations in nature (e.g. valleys and rivers), buildings, irrigation systems and industrial fluid-transport infrastructures. It is therefore of both practical and academic importance to understand and model the effects of the inclined or curved sidewalls of the channel on the flow of the GC.

The investigation of the flow field of high-Re GCs in channels with non-rectangular cross-sections is a relatively new topic. In the classical paper for the rectangular current, Benjamin (1968) also considered briefly a GC in a full circular channel (tube), but the analysis is restricted to the special non-dissipative flow only. Marino & Thomas (2009, 2011) and Monaghan *et al.* (2009) presented experimental results and some analytical modelling for a restricted family of cross-sections: a V-shaped valley (triangle plus rectangle) and power-law shapes (the width varies with height as $f(z) = bz^{\alpha}$, where b, α are positive constants). Ungarish (2012) gives a generalization of Benjamin's (1968) analysis of the steady-state current, and derives compact formulas for the front-jump conditions (the Froude number Fr and rate of dissipation) for a given cross-section-width function $f(z)$. Zemach & Ungarish (2013) have recently developed a one-layer shallow-water (SW) Boussinesq model for general $f(z)$, and presented finite-difference and analytical (for the initial slumping and long-time self-similar propagation) solutions for various geometries. The outcome of these investigations is both interesting and encouraging. First, it is now evident that the non-standard geometry introduces some non-trivial (and perhaps useful) changes in the behaviour of the GC; in particular, concerning the value of the speed of propagation, u_N, during the initial (slumping) stage and the rate of decay of u_N with time t at later stages. Second, it has been shown that this physical behaviour, for quite general $f(z)$ functions, is amenable to investigation and prediction by careful extensions of theoretical tools used for the modelling of the GC in the standard rectangular geometry. It therefore makes sense to attempt further progress in this direction.

One of the important gaps in the theoretical knowledge on this problem is the lack of a two-layer SW model. This is an essential tool in the understanding of the classical dam-break problem; in particular, for the full-depth lock-exchange flow. The available theoretical investigations of the lock-release time-dependent flow (Monaghan *et al.* 2009; Marino & Thomas 2011; Zemach & Ungarish 2013) use box models and one-layer SW models for Boussinesq systems. These approximations neglect the effect of the return flow in the ambient fluid. The box model postulates a horizontal interface over the entire length of the current, and is therefore unable to capture the initial dam-break and 'slumping' phases of propagation during which the speed is constant while the height of the interface changes dramatically over the length. The one-layer model correctly predicts the existence of the slumping phase, but it is well known (from the rectangular case) that the details of the flow field are unreliable when the current is not 'deep' in the ambient. A two-layer model is needed for a more reliable physical understanding and more accurate prediction of the flow in this case. The

https://doi.org/10.1017/jfm.2013.417 Published online by Cambridge University Press

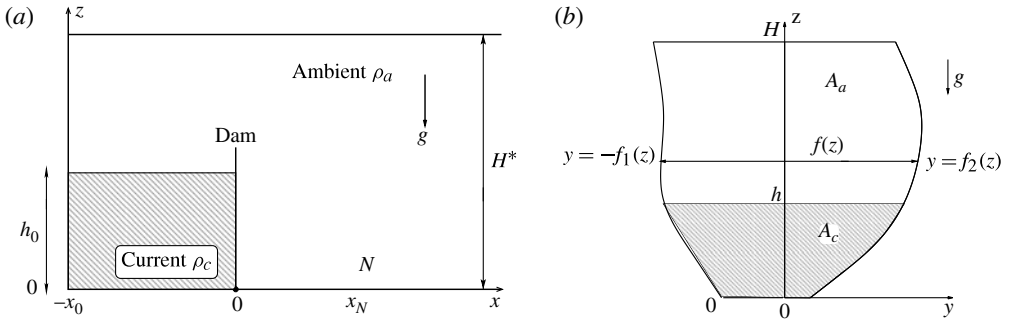


FIGURE 1. A schematic description of the lock-release (dam-break) problem. (*a*) The side view in the *xz* plane in the initial stage; (*b*) The cross-section at some *x* during propagation.

object of this work is to develop the two-layer model and obtain dam-break solutions in cases that clarify the effects of the returning flow in the ambient.

The typical geometry is sketched in figure 1. Let x be the horizontal coordinate along the channel, y the horizontal coordinate orthogonal to x and z the vertical coordinate pointing upwards. To be specific, the sidewalls are given by $y=-f_1(z)$ and $y=f_2(z)$, $0\leqslant z\leqslant H$. We shall see that the flow actually depends on the width function, $f(z)=f_1(z)+f_2(z)$, which is assumed continuous and positive (zero width at $z=0$ and/or $z=H$ is allowed).

Our investigation introduces a two-layer SW model. The formulation is in terms of the height h of the interface and the speed u (averaged over the area of the current) as functions of x and t (time). This allows the calculation of the position of the nose, $x_N(t)$. We focus attention on a current of fixed volume released from rest from a reservoir of length x_0 in which the position of the interface is at h_0; we emphasize that the cross-section of the reservoir is the same as that of the channel. The limitations of the classical SW model for a rectangular cross-section, which have been discussed widely in the literature, are also relevant in the present case. On the other hand, the two-layer model also has some good qualities, which we expect will carry over to our more complex configuration. The dam-break analysis by this model is an essential component in the understanding of experimental observations and rigorous solution of GCs in the Boussinesq and non-Boussinesq domains (see Rottman & Simpson 1983; Klemp, Rotunno & Skamarock 1994; Lowe, Rottman & Linden 2005; Rotunno *et al.* 2011; Ungarish 2011). Due to its good balance of mathematical formalism and physical ingredients, it is possible to extract by analytical means some useful clear-cut insights, and fairly good quantitative results, concerning the influence of the governing parameters, the speed of propagation, and the shape of the interface, as functions of x and t. Indeed, the previous investigations of the standard rectangular (or laterally unbounded) dam-break problem revealed several interesting and non-trivial effects that become pronounced when the return flow in the ambient is significant, such as the presence of internal jumps/bores and 'critical' restrictions on the speed of propagation. These effects are bound to carry over to the flow in the non-rectangular cross-section, but subject to modifications that are presently unknown. Our objective is to close this gap in the knowledge. We show that the two-layer SW model is the appropriate tool for working out the necessary extensions.

https://doi.org/10.1017/jfm.2013.417 Published online by Cambridge University Press

The formulation that we derive is applicable to a quite general cross-section function $f(z)$ (the main formal requirement is continuity in $[0, H]$, and the obvious $f(z) > 0$ in $(0, H)$). For definiteness, we shall present results for bottom currents in the following types of channels: (a) $f(z) = bz^{\alpha}$, where b is a positive constant and $0 < \alpha \leqslant 2$ (this geometry is referred to as the power-law cross-section); (b) $f(z) = b(H - z)^{\alpha}$, which is the channel of case (a) in upside-down position; (c) a trapezoidal cross-section; and (d) a circle (full and sector). The shapes considered here are interesting from the academic point of view, and their relevance to industrial and environmental applications seems feasible.

The structure of the paper is as follows. The equations and boundary conditions are derived in § 2. The essential components of the flow-field solution (backward-moving jump, cores, nose jump) are developed and discussed in § 3. In §§ 4–7, we illustrate the solutions for typical definite cross-sections: power-law, trapezoidal and circle (full and sector). Comparisons of the speed of propagation with available experiments are presented in § 8. Some concluding remarks are given in § 9. Some details of the solution, not included in the main text for brevity of presentation, are given in appendices A and B, while a brief discussion of the reflected bore is presented in appendix C.

2. Formulation

The two-layer model is formulated for the current that propagates on the $z = 0$ boundary. We shall use the notation ρ_c for the density of the current and ρ_a for the other fluid, the ambient. We consider incompressible, immiscible fluids, and assume that the effects of viscosity, turbulence and entrainment are negligible during the process under consideration. The horizontal axis is x, and the gravitational acceleration g acts in the negative z direction. The bottom and the top of the channel are at $z = 0$ and $z = H$. The fluid of the current is originally confined in a reservoir of length x_0 and height h_0, located adjacent to the boundary on which propagation occurs (see figure 1).

We use dimensional variables unless stated otherwise. The position of the interface is $z = h(x, t)$. The assumption that the interface has no inclination in the lateral y direction is justified because this is the initial situation in the hydrostatic lock from which the current is released, and subsequently there is no mechanism in our system that can enforce lateral sloshing. The flow satisfies the no-penetration condition on the boundaries of the channel. Initially, at $t = 0$, $h = h_0$ and $u = 0$. We assume a shallow current, which is relevant for $h_0/x_0 \ll 1$. We shall use the subscript a to denote the variables associated with the ambient fluid; for the current, we shall use no subscript or, when emphasis is necessary, we shall use c.

Let A, A_a and A_T denote the cross-section area of the current, the ambient and the total for the channel. The relevant definitions are as follows:

$$A = A(h) = \int_0^h f(z)\,\mathrm{d}z, \quad A_T = \int_0^H f(z)\,\mathrm{d}z, \quad A_a = A_T - A. \tag{2.1}$$

Note that

$$\frac{\partial A}{\partial x} = f(h)\frac{\partial h}{\partial x}; \quad \frac{\partial A}{\partial t} = f(h)\frac{\partial h}{\partial t}. \tag{2.2}$$

We introduce the averaged velocities $\bar{u}(x, t)$ for the current and $\bar{u}_a(x, t)$ for the ambient. The averaging is over the corresponding areas. The continuity equation for

https://doi.org/10.1017/jfm.2013.417 Published online by Cambridge University Press

the current expresses the observation that the local $\partial A/\partial t = f(h)(\partial h/\partial t)$ is balanced by $-\partial(A\bar{u})/\partial x$. This can be rewritten as

$$\frac{\partial h}{\partial t} + \bar{u}\frac{\partial h}{\partial x} + \frac{A}{f(h)}\frac{\partial \bar{u}}{\partial x} = 0. \tag{2.3}$$

For the ambient layer, continuity yields

$$\bar{u}_a A_a = -\bar{u}A. \tag{2.4}$$

The derivation of the momentum equations is an extension of the classical procedure for the rectangular case. Briefly, the procedure is as follows. Both fluids are in z-hydrostatic balance, and the pressure is continuous at the interface $z = h$ (except for the segments of vertical jumps). It is convenient to use the reduced pressure $(+\rho_a g z)$, denoted Π. The pressures in the ambient, and in the current, are

$$\Pi_a = \Phi(x,t); \quad \Pi = \Phi(x,t) + \Delta\rho g\,[h(x,t) - z]\,; \tag{2.5}$$

where $\Delta\rho = |\rho_a - \rho_c|$. The driving effect is concerned with the x-component of the pressure gradient:

$$\frac{\partial \Pi_a}{\partial x} = \frac{\partial \Phi(x,t)}{\partial x}; \quad \frac{\partial \Pi}{\partial x} = \frac{\partial \Phi(x,t)}{\partial x} + \Delta\rho g\frac{\partial h}{\partial x}. \tag{2.6}$$

The basic x-momentum inviscid equation is

$$\rho_i\left[\frac{\partial u}{\partial t} + \frac{\partial u^2}{\partial x} + \frac{\partial (uv)}{\partial y} + \frac{\partial (uw)}{\partial z}\right]_i = -\frac{\partial \Pi_i}{\partial x} \tag{2.7}$$

where the subscript i denotes the current and ambient. We eliminate the right-hand side by (2.6), and integrate the equation over the cross-section of the corresponding fluid. After some algebra, we obtain, for the averaged $\bar{u}_i(x,t)$, the following equations:

$$\rho_a\left[\frac{\partial A\bar{u}}{\partial t} + \frac{\partial A\bar{u}^2}{\partial x}\right]_a = -A_a\frac{\partial \Phi(x,t)}{\partial x}; \tag{2.8}$$

$$\rho_c\left[\frac{\partial A\bar{u}}{\partial t} + \frac{\partial A\bar{u}^2}{\partial x}\right] = -A\frac{\partial \Phi(x,t)}{\partial x} - A\Delta\rho g\frac{\partial h}{\partial x}. \tag{2.9}$$

Again, the variables with no subscript refer to the current.

Upon the elimination of the pressure term Φ, and use of the kinematic relationships (2.3)–(2.4), the last two equations can be combined into one effective x-momentum equation in terms of the variables $h(x,t)$ and $\bar{u}(x,t)$ of the current. Hereafter, we drop the overbar of the averaged u, and write the combined momentum equation as

$$\left(1 + \frac{\rho_a}{\rho_c}\frac{\varphi}{1-\varphi}\right)\frac{\partial u}{\partial t} + \left[1 - \frac{\rho_a}{\rho_c}\frac{\varphi(1+\varphi)}{(1-\varphi)^2}\right]u\frac{\partial u}{\partial x} + \left[\frac{\Delta\rho}{\rho_c}g - \frac{\rho_a}{\rho_c}\frac{1}{(1-\varphi)^3}\frac{f(h)}{A_T}u^2\right]\frac{\partial h}{\partial x} = 0, \tag{2.10}$$

where

$$\varphi = \varphi(h) = \frac{A}{A_T}. \tag{2.11}$$

The continuity equation (2.3) and the combined momentum equation (2.10) define the motion of the current in terms of $h(x,t)$ and $u(x,t)$. The geometry of the cross-section enters the formulation via the terms φ and $f(h)/A_T$.

https://doi.org/10.1017/jfm.2013.417 Published online by Cambridge University Press

In order to obtain realistic GC solutions, the system of equations must be subjected to appropriate boundary conditions. The initial conditions at $t = 0$ are $u = 0$ and the thickness of the current in the reservoir is $h = h_0$. Mathematically, a Riemann-type problem is expected: the position of the dam, $x = 0$, is a singularity from which perturbations in form of characteristics and/or jump discontinuities (shocks) start to propagate immediately after the removal (break) of the dam. These messengers move with finite speed backward, i.e. into the reservoir, and forward, i.e. away from the reservoir. Consequently, at a given t, only a finite domain of the fluid, say $x_L(t) \leqslant x \leqslant x_N(t)$, is activated; outside this domain, the initial no-motion conditions prevail. It is essential to determine the boundary conditions, or jump conditions, at the front and back of the activated domain. The solution of the SW equations (2.3)–(2.10) is of interest only inside this domain.

The vertical plane $x = x_N(t)$ that moves forward with the nose of the SW gravity current is treated as a discontinuity. The necessary jump condition is

$$|u_N| = Fr_U(\varphi_N)\left(\frac{\Delta\rho}{\rho_a}g\right)^{1/2} h_N^{1/2}, \tag{2.12}$$

where N denotes the nose, and Fr_U is the extension of Ungarish (2012) to Benjamin's Froude number function for a cross-section specified by $f(z)$. To be specific,

$$(Fr_U)^2 = \frac{2(1-\varphi)}{1+\varphi}\left[1 - \varphi + \frac{1}{hA_T}\int_0^h zf(z)\,\mathrm{d}z\right], \tag{2.13}$$

and we use it for $h = h_N, \varphi = \varphi_N$. As shown in that paper, energy dissipation considerations impose the restriction $[Fr_U/(1-\varphi)]^2 \leqslant 2$, which typically means that the area occupied by the current is limited to $\varphi \leqslant \varphi_{max}$ (or $a = h_N/H \leqslant a_{max}$); the equality sign corresponds to the energy-conserving, zero dissipation, situation. Roughly, the dependency of Fr_U on φ is like that of Benjamin's Fr on $a = h_N/H$: Fr_U decreases from $\sqrt{2}$ by a factor of ~ 2 when φ increases from 0 (a very deep current) to φ_{max}. That extension of Benjamin's analysis takes into account the flow in both the current and the ambient, and therefore the application of the jump condition (2.12)–(2.13) to the present two-layer SW model is justified (see Ungarish 2009 § 3.2).

We note that the geometry of the cross-section enters the formulation of both the equations of motion and the front condition u_N. The reduction of the present SW formulation to the rectangular case is obtained by letting $f(z) = W_0 = \text{const.}$, and hence $A_T = W_0 H, \varphi = h/H$. In this case, (2.13) recovers Benjamin's (1968) formula.

The condition at the backward-moving boundary, $x = x_L(t)$, is either a smooth rarefaction wave or a jump. This will be discussed in § 3.1.

The definition of the dimensionless variables is as follows. We introduce the reference width $W_0 = f(h_0)$ and reference area $W_0 h_0$. (In some cases, a different definition of W_0 may be convenient, such as h_0 or $f(h_0/2)$; this turns out to be quite flexible because the effect of W_0 actually cancels out in the subsequent calculations.) The reference speed U and time T are as in the classical case:

$$U = \left(\frac{\Delta\rho}{\rho_c}gh_0\right)^{1/2}; \quad T = \frac{x_0}{U}. \tag{2.14}$$

The x-lengths are scaled by x_0, while the vertical lengths are scaled by h_0. The switch from dimensional variables, denoted below by an asterisk, to dimensionless

https://doi.org/10.1017/jfm.2013.417 Published online by Cambridge University Press

variables, is summarized as follows:

$$\{x^*, f^*(z^*), A_i^*, z^*, h^*, H^*, t^*, u^*, \Pi^*\} = \{x_0 x, W_0 f(z), W_0 h_0 A_i, h_0 z, h_0 h, h_0 H, Tt, Uu, \rho_c U^2 \Pi\}, \tag{2.15}$$

where Π denotes the reduced pressure.

It is convenient to introduce the density ratio parameter R, of light to heavy fluids, in the range $(0, 1)$. The Boussinesq system corresponds to the limit $R \to 1^-$.

The present investigation can easily be adapted to a 'top' current: we just replace z with $\zeta = H - z$. We consider a current that propagates on the boundary $\zeta = 0$; $\zeta = h(x, t)$ is the position of the interface, which again represents the thickness of the current. We define the width function $\psi(\zeta) = f(H - \zeta)$, and we simply replace $f(z)$ with $\psi(\zeta)$ in the foregoing formulation. The interpretation of $\psi(h), A(h), \varphi(h)$ is straightforward. This change of geometry will also enter into the value of Fr_U. In this case, $\rho_c/\rho_a < 1$ and $R = \rho_c/\rho_a$. Otherwise, the equations of motion remain unchanged. In the Boussinesq case, the difference between the 'top' and 'bottom' currents is a result of the change of geometry only: a top-to-bottom change of the channel will change the propagation of the bottom current into that of the top current in the original geometry.

3. Outline of the current domain solution

We shall focus on the solution of a 'heavy' GC that propagates on the bottom of the channel. In this case, $\rho_c > \rho_a$, $R = \rho_a/\rho_c$ and the reference speed is

$$U = \left[\frac{\rho_c - \rho_a}{\rho_c} g h_0\right]^{1/2} = [(1 - R) g h_0]^{1/2} = [g' h_0]^{1/2}. \tag{3.1}$$

The variables $h(x, t)$ and $u(x, t)$ represent the thickness and the speed of a bottom current, scaled according to (2.15); g' is the reduced gravity.

The continuity equation (2.3) is in standard form, and the momentum equation (2.10) is reformulated by dividing by the coefficient of $\partial u/\partial t$ and rearrangement. This yields the dimensionless system of equations as follows:

$$\begin{cases} \dfrac{\partial h}{\partial t} + u\dfrac{\partial h}{\partial x} + \dfrac{A}{f(h)}\dfrac{\partial u}{\partial x} = 0; \\ \dfrac{\partial u}{\partial t} + D\dfrac{\partial h}{\partial x} + (1 - 2B) u \dfrac{\partial u}{\partial x} = 0, \end{cases} \tag{3.2}$$

where

$$B = \frac{R\varphi}{1 - \varphi}(1 - \varphi + R\varphi)^{-1}; \quad D = \left[1 - \varphi - R\left(\frac{1}{1 - \varphi}\right)^2 \frac{f(h)}{A_T} u^2\right](1 - \varphi + R\varphi)^{-1}. \tag{3.3}$$

We calculate the eigenvalues of the matrix that multiplies the $[h_x, u_x]$ column vector of the system (3.2), and the left-hand-side eigenvectors (see Ungarish 2009, appendix B). We assume that the eigenvalues are real and distinct, and the eigenvectors are a full set. By inspection and analogy with the standard rectangular case, we expect (and later confirm) that this assumption is relevant to geometries of practical interest. In such cases, the PDE system for $h(x, t), u(x, t)$ is hyperbolic, with characteristic

https://doi.org/10.1017/jfm.2013.417 Published online by Cambridge University Press

relationships and trajectories given by

$$\frac{\mathrm{d}h}{\mathrm{d}u} = \frac{1}{D}\left[Bu \mp \sqrt{(Bu)^2 + D\frac{A}{f(h)}}\right], \tag{3.4}$$

on

$$\frac{\mathrm{d}x}{\mathrm{d}t} = c_\pm = c_\pm(h,u) = u(1-B) \pm \sqrt{(Bu)^2 + D\frac{A}{f(h)}}. \tag{3.5}$$

We keep in mind that, for a given $f(z)$, the variable φ is a function of h. Also note that

$$\frac{f(h)}{A_T} = \varphi'(h) \quad \text{and} \quad \frac{f(h)}{A} = \frac{\varphi'(h)}{\varphi}. \tag{3.6}$$

For the rectangular cross-section, we obtain the reduction $f(z) = 1, A = h, A_T = H$ and $\varphi = h/H = a$.

The scaled nose-speed condition (2.12) reads

$$u_N = \frac{1}{R^{1/2}} Fr_U(\varphi_N) h_N^{1/2}. \tag{3.7}$$

The solution, in general, requires the integration of (3.4) to obtain $u(h)$ on certain characteristics. For these calculations we used a fourth-order Runge–Kutta method, with typically 500 steps between the 'initial' and 'final' points; the CPU time is insignificant.

The foregoing equations admit solutions of the following forms: (i) domains of constant h and u, referred to as cores, or constant-state regions – this can be verified by inspection; and (ii) fans of characteristics emanating from the dam at the start of the flow. The trajectories are $x = c_-(h_i, u_i)\cdot t$ or $x = c_+(h_i, u_i)\cdot t$. Here, h_i is the initial h condition on the specific ray in the fan, and u_i follows from the intersection with the $u(h)$ solution on the associated c_+ (or c_-) characteristic, or boundary condition. This fan, or expansion region, solution follows from the observation that c_- (or c_+) is constant for a fixed pair of h, u (see (3.5)), and the corresponding $\mathrm{d}h = \mathrm{d}u = 0$ satisfy the balance equation (3.4) on this characteristic. A necessary condition is that the $u(h)$ that intersects the fan emanates from a time-independent boundary condition. The characteristic fan yields a curved and inclined $h(x,t)$ portion of interface. The dam-break flow field is a combination of such cores and fans, until the moving fluid encounters an obstacle. The challenge is to determine the appropriate boundary and matching conditions between the domains, for a general shape of the channel's cross-section.

The one-layer model of Zemach & Ungarish (2013) corresponds to $B = 0, D = 1$, and hence the differences with the present two-layer results are expected to be small when $B \ll 1$ and $D \approx 1$. This occurs when $A_T \gg 1$, according to (3.3), where u is of order unity. In the one-layer case, there is a simple relationship between the velocities of the characteristics and that of the fluid, $c_\pm = u \pm [A/f(h)]^{1/2}$. Consequently, in practical geometries, the flow is of Type 1 (see figure 2(*a*)): the interface is matched smoothly to the reservoir by a rarefaction wave of velocity $c_-(1,0)$ at the left side of the activated domain, and then descends to the height $h_{core} = h_N$. The nose is subcritical ($u_N < c_+(h_N, u_N)$). Between the nose and the inclined portion of the interface there is a rectangular core of height h_N in which the fluid moves with u_N. The entire flow field can be obtained by integration of $\mathrm{d}u/\mathrm{d}h$ on a c_+ characteristic

https://doi.org/10.1017/jfm.2013.417 Published online by Cambridge University Press

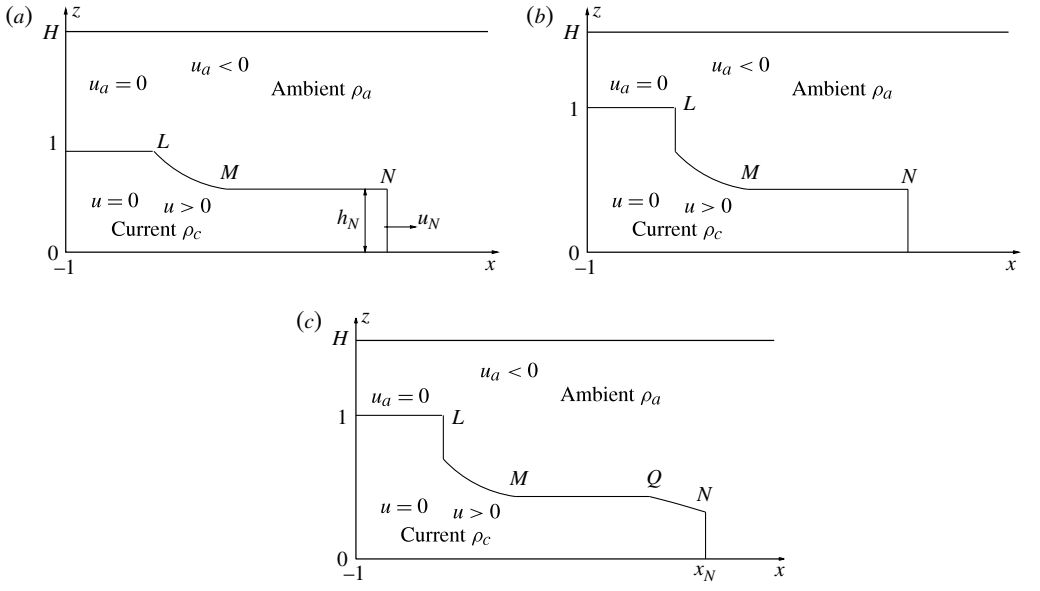


FIGURE 2. A schematic description of the types of flow fields. (*a*) Type 1: rarefaction wave propagating into the reservoir (position L) and subcritical nose (position N); (*b*) Type 2: jump at position L, subcritical nose; (*c*) Type 3: jump at position L, critical nose. Here, z is scaled with h_0, x with x_0. Point L denotes the transition from the reservoir to the activated (moving) domain, and N the nose on the opposite boundary of the activated domain; M denotes the left boundary of the core, and Q the left boundary of the expansion domain following the nose (when present).

from $(1, 0)$ initial conditions until intersection with the nose Froude condition, which determines (h_N, u_N).

The two-layer solution is of interest when deviations from the above-mentioned features show up. This occurs when the return flow is relatively important. The system becomes more rigid because the flow of the current produces a significant reaction of speed (and momentum) in the ambient. This is reflected by the fact that the behaviour of $c_\pm$ is complicated, and a more careful analysis of the boundary and matching conditions is necessary. There are conflicts between the standard dam-break flow and the propagation of perturbation, and some special features, with no counterpart in the one-layer model, appear. The shape of the interface at the connection with the reservoir may be a jump, instead of a smooth rarefaction wave (the propagation is into the reservoir). In addition, the nose may be critical, $u_N = c_+(h_N, u_N)$; in this case, the interface behind the nose is an expansion domain with a negative $\partial h/\partial x$ slope, instead of a core of constant h. It is therefore convenient to classify the currents as follows: Type 2 when a jump into the reservoir exists, but behind the nose there is a regular core with $u_N < c_+$; and Type 3 when both a jump into the reservoir and an expansion domain following a critical nose exist. The 'usual' SW current, with a rarefaction wave propagating into the reservoir and a subcritical nose, is defined as Type 1. The three types are sketched in figure 2.

In the standard rectangular Boussinesq case, the type (1, 2 or 3) of the flow is determined by the value of H: >2, 1.25–2, 1–1.25 (Ungarish 2009 §§ 5.3–5.4). Now this classification is complicated by the width function $f(z)$. For a general $f(z)$, other

https://doi.org/10.1017/jfm.2013.417 Published online by Cambridge University Press

arrangements of flow domains may exist. The equations of the characteristics contain the geometry of the cross-section, and thus can render patterns that contradict our 'intuition' built on rectangular geometry; in particular, the roots in these equations are prone to produce imaginary (non-physical) solutions for some combinations of the parameters. However, figure 2 provides a useful guide. The Boussinesq system and cross-section geometries considered in this work were, in almost all case, within Types 1–3. An exception, labelled Type 4, will be discussed in § 7. Note that some care is required in interpretation of the full-depth lock, $H = 1$, case, because the 'current' and the 'ambient' are interchangeable (as indicated by the 'lock-exchange' title widely attached to this configuration).

3.1. *Left-moving (into the reservoir) jump*

When the dam is removed at $t = 0$, a perturbation propagates into the reservoir of heavy fluid (upstream with respect to the current, to the left in figures 1(*a*) and 2).

As is known from the analysis for the rectangular cross-section, the smooth inclined part of the interface adjacent to the reservoir is a result of an expansion fan of the c_- characteristics. The smooth behaviour requires that the c_- characteristics maintain a well-arranged velocity spectrum: a characteristic at a larger h must propagate faster (in absolute value) than a characteristic at a smaller h, i.e. $\mathrm{d}|c_-|/\mathrm{d}h > 0$ (more conveniently expressed as $\mathrm{d}c_-^2/\mathrm{d}h > 0$). If this condition is not satisfied, the characteristics will intersect and the smooth $h(x)$ scenario will become inadequate.

The leading left-moving characteristics, which propagate the initial depression of the interface into the unperturbed fluid reservoir where $h = 1$, $u = 0$, are the test case. The initial motion is a small perturbation from the 'at rest' conditions; therefore we use $u \approx 0$, and (3.5), to estimate

$$c_-^2(h) = \frac{[1-\varphi(h)]\varphi(h)}{\varphi'(h)[1-\varphi(h)+R\varphi(h)]}. \tag{3.8}$$

We can thus calculate the value of $\mathrm{d}c_-^2/\mathrm{d}h$ at $h = 1$. When the sign of this result is positive, a smooth rarefaction wave propagates to the left; when negative, the perturbations with smaller h are able to overtake those closer to the top, and a jump develops.

An inspection of (3.8) provides an insight into the expected behaviour: c_- tends to 0 as φ approaches 1, which means that a back-moving jump is necessary to set the stagnant reservoir into motion when A of the current occupies almost all of the cross-section A_T. This is compatible with our experience in rectangular cross-section cases: a change of sign of $\mathrm{d}c_-^2/\mathrm{d}h$ occurs at some H_{crit} (=2 in Boussinesq systems (see Rottman & Simpson 1983; Klemp *et al.* 1994; Ungarish 2009), which marks the transition from the rarefaction-wave scenario (for $H > H_{crit}$) to the jump feature. In general, the right-hand side of (3.8) is not a simple expression in terms of h. The H_{crit} result now depends strongly on $f(z)$, and usually requires numerical evaluation. Again, for $H < H_{crit}$ the perturbations from smaller h, i.e. larger initial depression, tend to move faster to the left (into the reservoir). The depressed interface continues to steepen until it forms a jump of h and u, as sketched in figure 2(*b,c*). Some examples will be presented in §§ 4–7. We note in passing that the existence of such jumps in rectangular channels has been confirmed by experiments (see Rottman & Simpson 1983), although the measured H_{crit} was smaller than the theoretical prediction. The discrepancy can be attributed to the fact that the interface of a real current is affected by instabilities and shear, which tend to smooth out small-amplitude jumps. We think

https://doi.org/10.1017/jfm.2013.417 Published online by Cambridge University Press

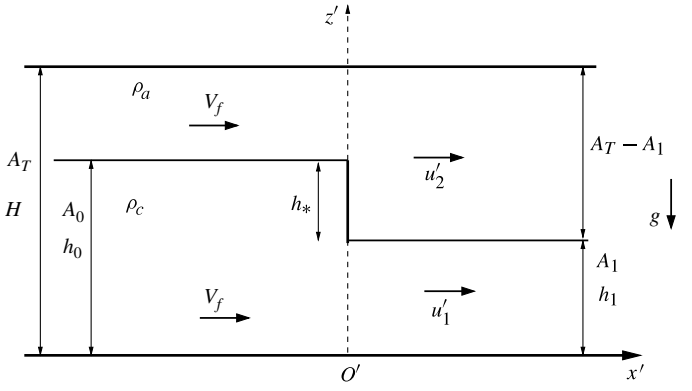


FIGURE 3. The flow in a control volume about the left-moving jump, as seen by an attached observer. The x coordinate is stretched; in a real system, the horizontal interface may be (slightly) inclined.

that a sharper distinction between the small-amplitude jump and a rarefaction wave at $H \approx H_{crit}$ can be achieved by Navier–Stokes simulation.

The discontinuity appears instantaneously in the SW framework. The task is to determine the height h_* and speed V_f, to the left, of this jump. It is convenient to use a frame of reference S' moving with the discontinuity; the x'-axis is on the bottom and directed to the right, like x; in the vertical direction, $z' = z$. Now, the flow about the jump is in a quasi-steady state, over short x' distances at least.

We refer to figure 3. The transformation of the velocity is $u' = u + V_f$, where the prime denotes the moving frame, and u is the velocity in the laboratory frame. We consider the balances for a x'-thin control volume attached to the jump. The subscripts l and r denote the left and right vertical (virtual) boundaries of this volume in figure 3. For the jump analysis, we use dimensional variables, unless stated otherwise. The subscripts 1 and 2 denote the variables in the lower and upper layers, respectively, to the right of the jump. The kinematic conditions are as follows. On the left, there is unperturbed fluid with $u = 0$, and hence $u' = V_f$, in both the heavy and the ambient fluid. On the right, we obtain from geometry and volume continuity considerations

$$A_1 + A_2 = A_T; \tag{3.9}$$

$$u_1'/V_f = \varphi_0/\varphi_1; \quad u_2'/V_f = (1-\varphi_0)/(1-\varphi_1); \tag{3.10}$$

where $\varphi_i = A_i/A_T$.

The pressure on the right and left of the jump is hydrostatic. On the left, the reduced pressure is

$$\Pi_l = \begin{cases} \mathscr{C} + \Delta\rho g(h_0 - z) & (\text{over } A_0) \\ \mathscr{C} & (\text{over } A_T - A_0); \end{cases} \tag{3.11}$$

where $\mathscr{C}$ is a constant and A_0 is the area of the current on the left.

On a streamline at the top, $z = H$, we apply Bernoulli's equation. In the S' frame, the flow is in steady state, and here we assume an ideal, non-dissipative streamline. This is consistent with our attempt to calculate the flow without using any adjustable constants, such as empirical energy losses. We obtain

$$\Pi_r(z = H) = \mathscr{C} + \tfrac{1}{2}\rho_S\left(V_f^2 - u_2'^2\right). \tag{3.12}$$

https://doi.org/10.1017/jfm.2013.417 Published online by Cambridge University Press

The subscript S of ρ emphasizes that this result has a singular behaviour for the full-depth lock case. In general, (3.12) is written for the ambient fluid with $\rho_S = \rho_a$. The $H = h_0$ case is an exception: on the left of the jump there is only heavy fluid, and the ambient fluid on the right is co-moving with the jump, i.e. $u_2' = 0$. The use of $\rho_S = \rho_c$ for this case renders $\Pi_r(z = H)$ as the appropriate stagnation pressure. The justification for the use of Bernoulli's equation at the upper boundary (for the layer of fluid that expands as it moves through the jump, and hence a stagnation-like increase of the pressure occurs) can be found in Ungarish (2011) and Borden, Meiburg & Constantinescu (2012).

The pressure on the right of the jump can now be expressed as

$$\Pi_r = \begin{cases} \mathscr{C} + \frac{1}{2}\rho_S\left(V_f^2 - u_2'^2\right) + \Delta\rho g(h_1 - z) & (\text{over } A_1) \\ \mathscr{C} + \frac{1}{2}\rho_S\left(V_f^2 - u_2'^2\right) & (\text{over } A_T - A_1). \end{cases} \tag{3.13}$$

Finally, we employ the flow-force balance for the moving control volume

$$\iint_{A_T} [\rho u'^2 + \Pi]_l \, \mathrm{d}A = \iint_{A_T} [\rho u'^2 + \Pi]_r \, \mathrm{d}A. \tag{3.14}$$

We substitute the expressions (3.9)–(3.11) and (3.13) into (3.14). The flow-force balance equation can be cast, with the aid of the continuity equations (3.10) (expressed as $A_0 V_f = A_1 u_1'$ and $(A_T - A_0)V_f = (A_T - A_1)u_2'$), in the convenient form

$$\begin{aligned} &A_0\rho_c V_f(u_1' - V_f) + (A_T - A_0)\rho_a V_f(u_2' - V_f) + A_T\frac{1}{2}\rho_S(V_f^2 - u_2'^2) \\ &= \Delta\rho g\left[\iint_{A_0}(h_0 - z)\,\mathrm{d}A - \iint_{A_1}(h_1 - z)\,\mathrm{d}A\right]. \end{aligned} \tag{3.15}$$

The first two terms on the left-hand side represent the momentum change of the streams of the current and ambient passing the jump from left to right. The third term is the contribution of the stagnation pressure, while the terms on the right-hand side are the contribution of the hydrostatic pressure. Note that by (3.10), the velocities $u_{1,2}'$ can be eliminated in terms of V_f; moreover, in the final balance, the velocities appear only at the second power. After some algebra (see appendix A), we obtain

$$V_f^2 = \frac{\Delta\rho}{\rho_c} g \frac{q}{s}, \tag{3.16}$$

where

$$q = h_0\varphi_0 - h_1\varphi_1 - \frac{1}{A_T}\int_{h_1}^{h_0} z f(z)\,\mathrm{d}z; \tag{3.17}$$

$$s = (\varphi_0 - \varphi_1)\left[\frac{\varphi_0}{\varphi_1} - R\frac{1 - \varphi_0}{1 - \varphi_1} + \frac{1}{2}\left(\frac{\rho_S}{\rho_c}\right)\frac{2 - \varphi_0 - \varphi_1}{(1 - \varphi_1)^2}\right]. \tag{3.18}$$

Recall that ρ_S is ρ_a when $H > 1$, and ρ_c when $H = 1$.

This explicit result of the speed of the jump for a given drop of height from h_0 to h_1, although derived in the context of our particular problem, actually has quite a wide range of applicability: Boussinesq and non-Boussinesq systems, in standard rectangular and non-rectangular cross-section channels, for jumps propagating into full-depth and part-depth reservoirs. This can be considered as a generalization of many useful previous results for the relation between the speed and height of a hydraulic

https://doi.org/10.1017/jfm.2013.417 Published online by Cambridge University Press

jump or bore in a two-layer system; in particular, Benjamin's formula and the jump conditions of Klemp *et al.* (1994), Klemp, Rotunno & Skamarock (1997) and Borden *et al.* (2012). The calculation of V_f involves integrals of $f(z)$ and $zf(z)$. In the classical case $f(z) = \text{const.}$, both s and q are readily simplified. In the Boussinesq case, $R = 1$ and $\rho_S/\rho_c = 1$, which also allows further simplification of the expressions given above.

Next, we scale the variables according to (2.14)–(2.15). We define the dimensionless height of the jump as

$$h_* = 1 - h_1. \tag{3.19}$$

What is important to our analysis is that we are now able to calculate the value of V_f for a given jump height, h_* (positive and smaller than 1). This result is the 'first equation' for the jump. Evidently, a physical solution is possible only when the right-hand side of (3.16) is positive. This is consistent with our previous observation that a jump appears when geometric constraints prohibit the propagation of a rarefaction wave into the reservoir.

The 'first equation' is a necessary condition. However, since this is one equation for two unknowns (the speed and height of the jump), the solution is not unique. Physically acceptable speed results are usually obtained for a domain of positive and physically acceptable h_*. We need a 'second equation' to determine the value of h_* in our flow field. We recall that the jump develops because of mismatched dependencies of c_- on h in the propagation of the depression emanated by the dam-break. This is resolved when the jump is also the fastest characteristic of the neighbouring expansion fan. We therefore write the second equation for the jump as

$$V_f = |c_{-r}|. \tag{3.20}$$

We emphasize that c_{-r} is calculated using (3.5) with $u = u_1$ and $h = h_1 = 1 - h_*$. This jump moves with critical speed into the reservoir, and is therefore the fastest jump that may appear at the left boundary of the activated domain. Here, the jump governed by (3.16)–(3.20) is loosely called a 'free jump,' because its properties are determined by local conditions and it is free to attain the optimal speed in the given geometry.

It is well known that a jump is associated with an energy imbalance that is usually referred to as dissipation. The calculation for the non-rectangular cross-section is as follows. We again use the moving S' system and a thin control volume attached to the jump. The rate of dissipation of energy of the jump is defined as

$$\begin{aligned}\dot{\mathscr{D}} = &-\iint_{A_T}\left\{\left[\frac{1}{2}\rho u'^2 + \Pi + (\rho - \rho_a)gz\right]u'\right\}_{in}\mathrm{d}A \\ &+\iint_{A_T}\left\{\left[\frac{1}{2}\rho u'^2 + \Pi + (\rho - \rho_a)gz\right]u'\right\}_{out}\mathrm{d}A.\end{aligned} \tag{3.21}$$

The *in* and *out* subscripts are with respect to an observer inside the control volume. The last term in the integrals represents the potential energy, because the pressure Π is reduced with $+\rho_a gz$.

We use the same pressure terms and continuity equations as for the flow–force balance above. It turns out that the potential-energy terms cancel out with the $\Delta\rho gz$ terms of Π on both sides of the jump. In the spirit of (3.15), we can cast the balance (3.21), in dimensional form, as

$$\begin{aligned}\dot{\mathscr{D}} = &-A_0\rho_c V_f \tfrac{1}{2}(V_f^2 - u_1'^2) - (A_T - A_0)\rho_a V_f \tfrac{1}{2}(V_f^2 - u_2'^2) \\ &+A_T V_f \tfrac{1}{2}\rho_S(V_f^2 - u_2'^2) - A_0 V_f \Delta\rho g(h_0 - h_1).\end{aligned} \tag{3.22}$$

https://doi.org/10.1017/jfm.2013.417 Published online by Cambridge University Press

The dimensionless form of $\dot{\mathscr{D}}$ is obtained by scaling with $(1/2)\rho_c U^3 A_0$ (the typical rate of pressure work of the nose against the ambient fluid). The calculation of $\dot{\mathscr{D}}$ is performed after the solution of the jump, and hence V_f and h_1 are known. Some details are given in appendix A.

An inspection of (3.15) and (3.22) indicates that the fulfilment of the no-acceleration condition of the control volume is unlikely to also fulfil the no-dissipation condition. In general, $\dot{\mathscr{D}} \neq 0$ is expected. Only jumps with $\dot{\mathscr{D}} \leqslant 0$ are physically acceptable, because no source of energy is available to justify a positive energy gain of the fluid that passes the jump.

Even if the energy restriction is satisfied, the free jump may be an unattainable solution. We must keep in mind that in a realistic dam-break flow, the jump is a component of a more complicated arrangement than sketched in figure 3. It is therefore necessary to verify that the presence of the free jump on the left boundary of the activated domain is compatible with the conditions inside the domain, and at the opposite boundary (nose of the current). This we check using a c_+ characteristic from the jump into the current, up to the nose. If some incompatibility is detected, it may indicate that the jump is restricted to moving with a lower speed, i.e. is subcritical with respect to the c_- characteristic. In other words, the jump satisfies the 'first equation' but not the 'second' one. Speed corrections by some iterations of the flow field domains can be attempted until compatibility is achieved. (A simple 'correction' is to start the solution from the other boundary – the nose – with the assumption that a free jump occurs there.) This procedure was applied in the solutions presented below.

Finally, we emphasize that the speed and height of the left-moving jump (into the reservoir) of dense fluid (see figures 1(*a*) and 2) depend only on H and $f(z)$. Consequently, this is a time-independent effect, until this jump reaches the left-side endwall $x = -1$. Then, the jump is reflected: the velocity changes direction, and the upper fluid layer is thicker to the left and thinner to the right of the discontinuity, as discussed briefly in appendix C.

3.2. *Critical nose speed and height*

The nose jump of the heavy current satisfies the front condition $u = Fr_U h^{1/2}/R^{1/2}$, and a second equation is needed to determine the values of $h = h_N$ and $u = u_N$.

A free propagation with the critical speed $u_N = c_+$ may develop. This is the maximum available speed, or choked motion, for the heavy current. Equation (3.5) shows that the sign of D is the discriminant between the conditions of u with respect to c_+. Combining (3.5) with (3.3), we can write

$$\text{sign}(c_+ - u) = \text{sign}[(1-\varphi)^3 - \varphi' R u^2]. \tag{3.23}$$

(Recall that $\varphi = \varphi(h)$.)

The critical speed $u = c_+$ is achieved when $u^2 = (1-\varphi)^3/(R\varphi')$. On the other hand, at the nose $u = Fr_U(\varphi) h^{1/2}/R^{1/2}$. The intersection of these two conditions is

$$(1-\varphi)^3 = Fr_U^2(\varphi)(h\varphi'), \tag{3.24}$$

independent of R. The solution, strongly dependent on $f(z)$ of the cross-section, determines the height h_N and speed u_N of the critical nose. Tests with various 'plausible' functions indicate that the critical nose effect appears only for H close

https://doi.org/10.1017/jfm.2013.417 Published online by Cambridge University Press

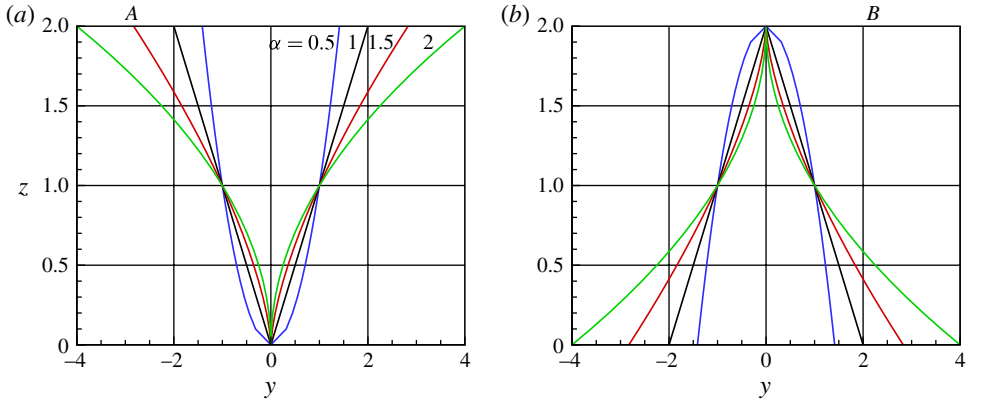


FIGURE 4. (Colour online) A schematic description of the power-law $f(z) = z^{\alpha}$ (case A) and $f(z) = (H - z)^{\alpha}$ (case B) geometries, for $H = 2$ and $\alpha = 0.5, 1, 1.5, 2$ (online: blue, black, red and green).

to 1 (as in the rectangular geometry), but we could not find a general proof or justification for this observation.

When the front jump at $x = x_N(t)$ is free (i.e. moves with the critical speed), the nose is followed by an expansion domain with a curved interface (see figure 2(*c*)). When the jump is not free, the 'second condition' at the right boundary is provided by $u(h)$ on a c_+ characteristic from the left boundary, and u_N is smaller than the critical value. We found that the energy restriction associated with the Fr_U condition, $a = h_N/H \leqslant a_{max}$, is satisfied in both critical and subcritical cases for all the configurations tested in this work.

4. Test case A: $f(z) = bz^{\alpha}$

Here, we illustrate the solution for realistic test cases: Boussinesq bottom currents in channels of the form $f(z) = bz^{\alpha}$, $0 \leqslant z \leqslant H$ (dimensional), where b, α are positive. This is the prototype of expanding geometry (as seen from the current at the bottom – see figure 4(*a*)). These configurations have been considered before in the literature (Monaghan *et al.* 2009; Marino & Thomas 2011; Zemach & Ungarish 2013), but a two-layer SW solution was not presented. For $\alpha = 1$, we obtain the simple '$\triangledown$' triangular channel.

An advantage of this width function, as also noted in the previous works, is that the rectangular cross-section results are recovered by simply setting $\alpha = 0$ in the more general solution. This is because we interpret the width function for $\alpha = 0$ as $f(z) = z^0 = W_0 = \text{const.}$ for $z \geqslant 0$.

The scaling width is $W_0 = bf(h_0)$, and the scaling speed is $(g'h_0)^{1/2}$. The following discussion is in dimensionless form (unless stated otherwise). The dimensionless H is the height of the channel scaled with h_0.

In dimensionless form, $f(z) = z^{\alpha}$, $0 \leqslant z \leqslant H$. Let $a = h/H$. It follows from the definitions that $A_T = H^{\alpha+1}/(\alpha+1)$; $\varphi = a^{\alpha+1}$; $A/f(h) = h/(\alpha+1)$; $f(h)/A_T = (\alpha+1)/H$; and

$$(Fr_U)^2 = 2\frac{(1 - a^{1+\alpha})}{1 + a^{1+\alpha}}\left(1 - \frac{1}{2+\alpha}a^{1+\alpha}\right). \tag{4.1}$$

https://doi.org/10.1017/jfm.2013.417 Published online by Cambridge University Press

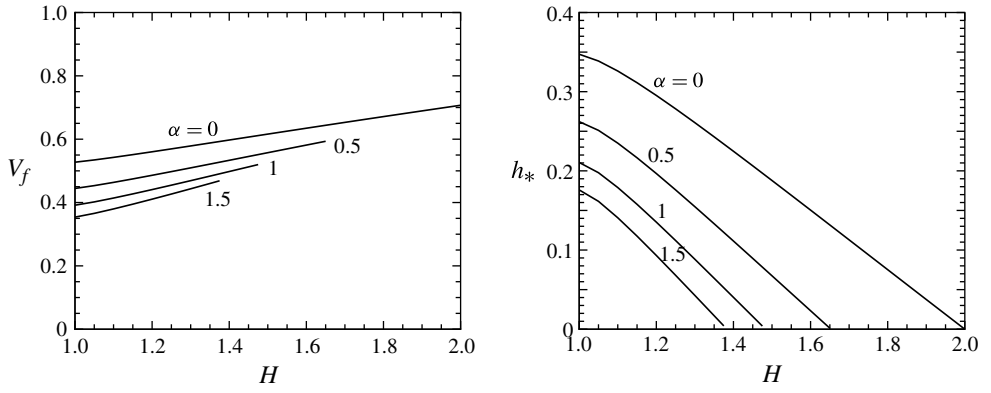


FIGURE 5. V_f and h_* of a left-moving free jump as functions of H for various α. Test case A.

Consider the formation of the left-moving jump into the reservoir. Using (3.8) with $R = 1$, we obtain

$$c_-^2 = \frac{1}{\alpha + 1}\left(1 - \frac{h^{\alpha+1}}{H^{\alpha+1}}\right) h \tag{4.2}$$

and hence $\mathrm{d}c_-^2/\mathrm{d}h < 0$ for $h/H > [1/(2+\alpha)]^{1/(\alpha+1)}$. Consequently, a jump will appear for channels with

$$H < H_{crit} = (2+\alpha)^{1/(\alpha+1)}. \tag{4.3}$$

The corresponding $H < 2$ restriction for the rectangular case $\alpha = 0$ is well known (Rottman & Simpson 1983; Klemp *et al.* 1994); in geometries with $\alpha > 0$, the area of the return flow expands for $z > h$, and hence the restriction becomes milder as α increases.

Using the equations (3.16)–(3.20), we calculated the speed and height of the free jump (see figure 5). (The presented results are energetically acceptable, $\dot{\mathscr{D}} \leqslant 0$).

We note that the height of the jump becomes very small (below 10^{-3}, close to 0 in the resolution of the plots) for values of H below H_{crit} predicted by (4.3); this effect becomes more pronounced as α increases. For example, for $\alpha = 1$, the calculations show that the jump is already quite insignificant, at $h_* \approx 1.2 \times 10^{-3}$, for $H = 1.48$; while the theoretical $H_{crit} = \sqrt{3} = 1.73$. Therefore, for the $\alpha = 1$ case, the SW solution with a rarefaction wave propagating into the reservoir is also valid (or at least a very good approximation) for $1.48 < H < 1.73$; this has been verified by the integration of the equations on the characteristics. A similar trend (i.e. the predicted H_{crit} is not sharp) also shows up in the other geometries tested in this paper. Our tentative explanation for this effect is as follows. Our derivation of H_{crit} assumes c_- characteristics in a $u = 0$ domain (see (3.8)); therefore, in a realistic flow with $u > 0$, a small deviation from the theoretical H_{crit} result could be expected. On the other hand, it is plausible that this non-sharp behaviour of the jump close to H_{crit} lacks physical significance, because in a real system a jump of small amplitude at the interface is unavoidably smeared out by the local instabilities and shear. The net outcome is that in experiments, the jump in the reservoir domain can be sharply observed only for values of H below the predicted H_{crit}. There is apparent consistency with the present calculations, but for different reasons.

https://doi.org/10.1017/jfm.2013.417 Published online by Cambridge University Press

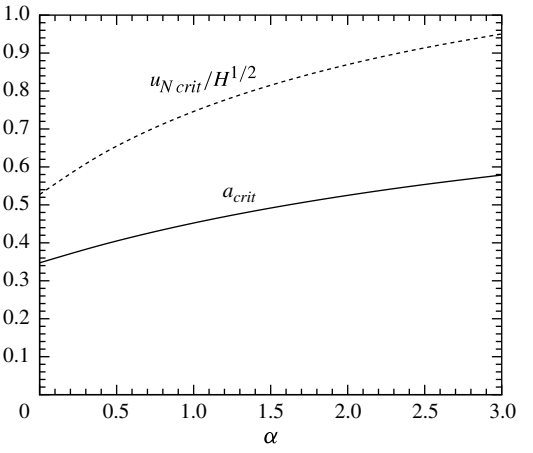


FIGURE 6. The critical nose a_{crit} and $u_{Ncrit}/H^{1/2}$ as functions of α. Test case A.

The critical nose condition $(1-\varphi)^3 = Fr_U^2(\varphi)(h\varphi')$ yields, after some algebra and use of (4.1), the condition

$$(1-a^{1+\alpha})^3 = 2\frac{(1-a^{1+\alpha})}{1+a^{1+\alpha}}\left(1-\frac{1}{2+\alpha}a^{1+\alpha}\right)(1+\alpha)a^{1+\alpha}. \tag{4.4}$$

The solution, a_{crit}, for a given α determines the maximal value of h_N/H that can be attained in lock release. This also determines the maximal speed, $u_{N\,crit} = Fr_U(a_{crit})\,a_{crit}^{1/2}\,H^{1/2}$. Typical results are shown in figure 6.

The calculation of the flow field requires integration of the characteristic equations. This we illustrate for the full-depth-lock $H=1$ case (the 'lock-exchange' problem). The rectangular-channel case has received a great deal of attention (Rottman & Simpson 1983; Klemp *et al.* 1994; Lowe *et al.* 2005; Rotunno *et al.* 2011; Ungarish 2011), and it is therefore interesting to extend the knowledge to the non-rectangular cross-section geometry. Here, we consider the Boussinesq $R=1$ case, and investigate the influence of α; the rectangular case corresponds to $\alpha=0$.

We start with the $\alpha=0$ case. This implies full symmetry between the light and heavy fluids (see figure 7). At $t=0$, free jumps, of height 0.347, are formed at the positions $x=0\pm$, and then propagate to the right and left with the same speed, $u_N = V_f = 0.527$. This is a Type 3 flow field: there is a left-moving jump into the reservoir of dense fluid, and the nose of the current moves with critical speed. In the centre of the activated fluid domain there are rectangular cores where the fluids have thickness 1/2 and speed 0.475 (absolute value). The points M and Q mark the boundaries of this region; these points move with the velocities of the characteristics from the dam to these points, c_M and c_Q, respectively (see table 1). The cores are matched to the jumps by expansion domains produced by fans of characteristics. Consider, for example, the lower heavy fluid: the interface LM corresponds to an expansion fan of c_- characteristics that originated at $x=0^-, t=0^+$. A c_+ characteristic from the left-moving jump (position L) propagates forward into the moving fluid, and carries the $u(h)$ values given by the integration of (3.4) with the initial conditions $h=0.653,\ u=0.281$; in particular, $u(0.500)=0.475$, the value in the core. The QN domain is the counterpart of LM for the c_+ characteristics from $x=0^+, t=0^+$; here, a c_- characteristic carries information from the right-moving

https://doi.org/10.1017/jfm.2013.417 Published online by Cambridge University Press

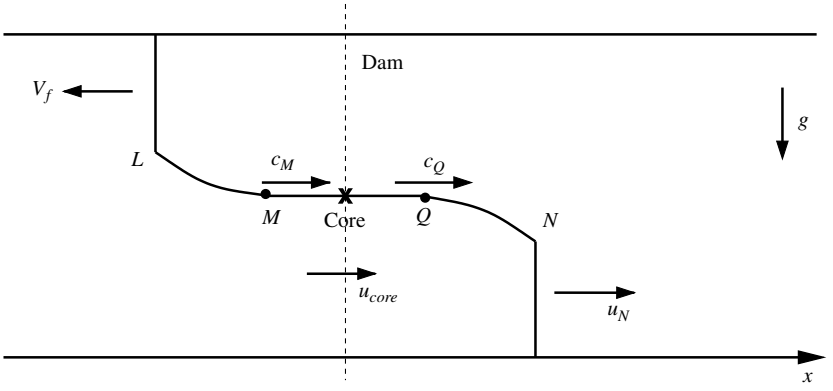


FIGURE 7. A schematic description of the $H = 1$ current for the classical Boussinesq rectangular case. The point on the interface marked '$\times$' is stationary, at the position of the dam. In this case, $V_f = u_N = 0.5273$, $-c_Q = c_M = 0.157$; $h_X = h_{core} = 1/2$.

α	h_*	V_f	h_X	h_{core}	u_{core}	c_M	c_Q	h_N	u_N	Type
0	0.347	0.527	0.500	0.500	0.475	−0.157	0.157	0.347	0.527	3
1	0.211	0.392	0.629	0.470	0.744	0.372	0.696	0.452	0.746	3
2	0.151	0.325	0.722	0.495	0.867	0.546	*	0.495	0.867	2

TABLE 1. Flow field properties for $f(z) = z^\alpha$, $H = 1$, as function of α; see figures 7–8. The asterisk (*) in the c_Q column means that point Q is virtual because the nose is subcritical.

front (position N) back into the moving fluid. The solution for this case has been reported previously (e.g. Klemp *et al.* 1994; Ungarish 2010).

Now consider the $\alpha = 1$ case. The previous symmetry between the lower and upper fluids is lost, because they propagate into different geometries (as seen from the boundary on which the fluid propagates away from the reservoir). To find the necessary modification, we first consider the dynamics of the jumps. We find that the left-moving free jump is weaker for $\alpha = 1$: $V_f = 0.3915$ and $h_* = 0.2106$. We perform integration of $\mathrm{d}h/\mathrm{d}u$ (or $\mathrm{d}u/\mathrm{d}h$) on a c_+ characteristic (see (3.4)), starting with the conditions in the lower fluid to the right of the jump, $(h, u) = (0.7894, 0.2367)$, in the direction of decreasing h and increasing u. We check when the resulting $u(h)$ intersects the front condition $Fr\, h^{1/2}$; we find that this occurs at a supercritical point where $u > c_+$. This means that the nose is critical, with $(h_N, u_N) = (0.452, 0.746)$ calculated as explained above. This is again a significant quantitative difference compared with the $\alpha = 0$ conditions $(0.347, 0.527)$. However, the flow field is still of Type 3. We integrate $\mathrm{d}u/\mathrm{d}h$ on a c_- characteristic, starting with the conditions at the nose, until intersection with $u(h)$ on the previously solved c_+ characteristic is achieved. This intersection determines the conditions in the core. The results are summarized in table 1 and figure 8. The difference between the heights and speeds of the core and nose are small for $\alpha = 1$, and much smaller than in the $\alpha = 0$ case. This indicates that a further slight increase of α will cause a transition to Type 2 flow. Additional

https://doi.org/10.1017/jfm.2013.417 Published online by Cambridge University Press

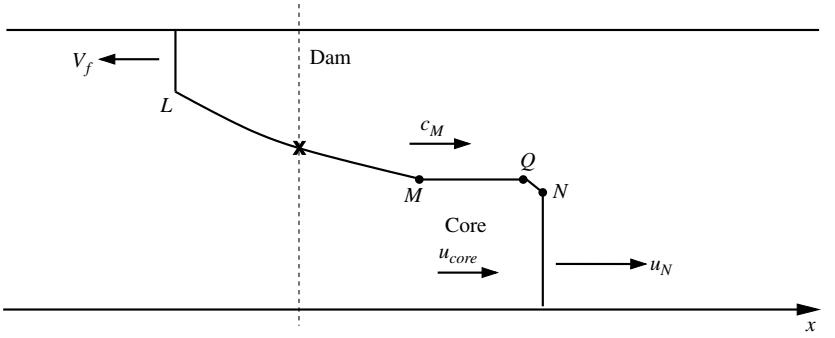


FIGURE 8. A schematic description of the $H = 1$ current for $f(z) = z$ (test case A, $\alpha = 1$). Here, $V_f = 0.392$, $h_* = 0.211$, and $u_N = 0.746$. (For larger α, point Q approaches point N, and the flow becomes of Type 2 for $\alpha > 1.27$.).

solutions (not displayed here) confirm that for $\alpha > 1.27$, we obtain subcritical u_N, i.e. the domain QN is not present (and point Q is at a virtual position in front of point N).

For $\alpha = 2$, the height of the left-moving jump is reduced to $h_* = 0.151$. The $u(h)$ result on the c_+ characteristic intersects the $Fr\, h^{1/2}$ condition at a subcritical point $(h, u) = (0.495, 0.867)$, where $c_+ = 0.952$. The results are summarized in table 1.

The asymmetry trend introduced by the non-rectangular cross-section effects is clear: for a given h, when α increases, the current at the bottom is exposed to a larger volume of ambient fluid. The analogy is with an increase of H in a rectangular cross-section. Indeed, when α increases, the left-moving jump becomes weaker, and the QN expansion zone following the heavy nose, with an inclined interface, shrinks (and actually disappears for $\alpha > 1.27$). The same trend is known to occur in a rectangular channel when H increases. The details given in table 1 provide a fairly complete description of the shape and speed of the current for a given $f(z) = bz^\alpha$ cross-section geometry, until the left-moving free jump hits the left endwall or the right-moving jump hits the right endwall.

5. Test case B: $f(z) = b(H - z)^\alpha$

Here, we illustrate the solution for another family of test cases: Boussinesq bottom currents in channels of the form $f(z) = b(H - z)^\alpha, 0 \leqslant z \leqslant H$ (dimensional), where b, α are positive . This is the prototype of contracting geometry (as seen from the current). We note that test cases A and B are connected: the channel in B is an inverted (top-to-bottom) channel A (see figure 4). In particular, for $\alpha = 1$ we obtain the simple '△' triangular cross-section. Therefore, a bottom Boussinesq current in A can be regarded as a top (light) current in B (and vice versa). In this cross-section geometry, $\varphi = 1 - (1 - a)^{1+\alpha}$; $A/f(h) = H\varphi/[(1 + \alpha)(1 - a)^\alpha]$; and

$$Fr_U^2 = \frac{2}{2 + \alpha} \frac{(1 - a)^{1+\alpha}}{a[2 - (1 - a)^{1+\alpha}]}[1 - (1 - a)^{2+\alpha}]. \tag{5.1}$$

Using (3.8) with $R = 1$, we obtain

$$c_-^2 = \frac{H}{\alpha + 1}\left[1 - (1 - a)^{\alpha+1}\right](1 - a) \tag{5.2}$$

https://doi.org/10.1017/jfm.2013.417 Published online by Cambridge University Press

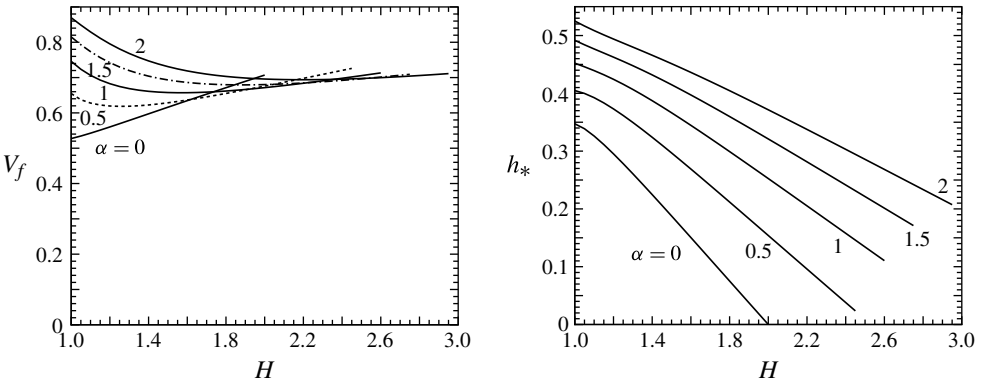


FIGURE 9. Test case B. V_f and h_* of a left-moving free jump as functions of H for various α.

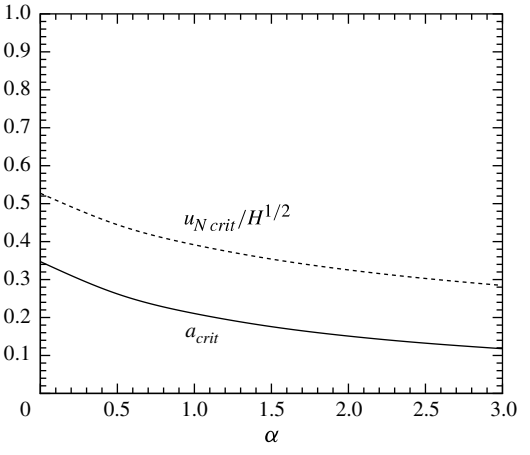


FIGURE 10. Test case B. a_{crit} and $u_{Ncrit}/H^{1/2}$ as functions of α.

where $a = h/H$. The transition point to $\mathrm{d}c_-^2/\mathrm{d}h < 0$ provides

$$H < H_{crit} = \left[1 - \left(\frac{1}{2+\alpha}\right)^{1/(\alpha+1)}\right]^{-1}. \tag{5.3}$$

The results for the speed and height of the jump are shown in figure 9.

The critical nose condition (3.24) yields

$$(1-a)^{3(1+\alpha)} = Fr_U^2(\varphi)(1+\alpha)(1-a)^{\alpha}a \tag{5.4}$$

and the results for a_{crit} and $u_{N\,crit}$ are shown in figure 10. The difference compared with case A (figure 6) is as expected: in the contracting cross-section, the return flow of the ambient is stronger than in the expanding cross-section. Consequently, there is a more pronounced choking effect in the former case.

Consider the full-depth $H = 1$ case. We argue that this flow is like a lock exchange, with the solution presented in the previous section for the geometry $f(z) = z^{\alpha}$. Let us return to test case A. The 'light' fluid there encounters the geometry $(1-\zeta)^{\alpha}$, where ζ

https://doi.org/10.1017/jfm.2013.417 Published online by Cambridge University Press

is the coordinate from the upper boundary into the fluid. The buoyancy pushes the light fluid in the $-\zeta$ direction. In the Boussinesq case, this is exactly the geometry and driving-force situation to which the bottom current in the test B case with $H = 1$ is subjected. Therefore, the flows of the light/heavy fluids in test case A interchange in test case B. To be specific, in test case B, the bottom current propagates with (h_N, u_N) given by (h_*, V_f) of case A for the same value of α; the backward-moving jump propagates with (h_*, V_f) given by (h_N, u_N) of case A. The other details of the flow field are also readily refitted.

It is interesting to note that now the backward-moving jump (into the reservoir) is free (critical) for $\alpha < 1.27$; in this case the flow is of Type 3. However, for larger values of α, $|V_f| < |c_-|$, and the jump leaves behind a straight interface, not a curved one. This is a variation of the Type 3 flow (with point M below L in figure 2*c*) that suggests the possibility of experimental verification.

6. Test case C: trapezium

Here, we consider the trapezium $f(z) = (d + z)/(d + 1)$ (dimensionless), where $d > 0$. This is an intermediary between the triangle $f(z) = z$ (of test case A, with $\alpha = 1$) and the classical rectangle $f(z) = 1$. We expect that as the value of d increases, the latter geometry becomes dominant. The more detailed calculations confirm this expected trend.

Recall that we are using dimensionless variables: the heights are scaled with h_0, and the width with that of the interface in the lock. Note that $f(1) = 1$. The dimensionless height of the channel is H.

Let $\delta = d/H$, and, again, $a = h/H$. We obtain

$$f(h) = H(\delta + a)/(d + 1); \quad A = H^2 a(\delta + a/2)/(d + 1); \quad A_T = H^2(\delta + 1/2)/(d + 1); \tag{6.1}$$

and hence

$$\varphi = a\frac{\delta + a/2}{\delta + 1/2}. \tag{6.2}$$

The use of (2.13) and the previous definitions yield, for the Froude number,

$$Fr_U^2 = \frac{2(1-\varphi)^2}{1+\varphi}\left[1 + \frac{a}{1-\varphi}\,\frac{\delta/2 + a/3}{\delta + 1/2}\right]. \tag{6.3}$$

For $\delta \to \infty$, we recover the classical rectangular cross-section results; and for $\delta = 0$, we recover the '$\triangledown$' triangular cross-section results (case A with $\alpha = 1$).

The analytical prediction of the domain of existence of the left-moving jump is cumbersome. However, we know that such a jump appears in the triangular and rectangular cross-section geometries for H smaller than $\sqrt{3}$ and 2, respectively. By numerical calculations, we indeed found, in the region indicated by these bounds, physically acceptable solutions of the jump balances derived in § 3.1; see figure 11.

Figure 11 shows the speed and height of the left-moving free jump in a trapezoidal cross-section. As d increases: the backward-moving jump becomes more prominent, and its speed increases. However, the dependency on d is significant only for $d \lesssim 2$. The results for $d = 3$ differ little from those of $d = 100$; the solution for the latter reproduces the perfect rectangle case to within a negligible discrepancy.

https://doi.org/10.1017/jfm.2013.417 Published online by Cambridge University Press

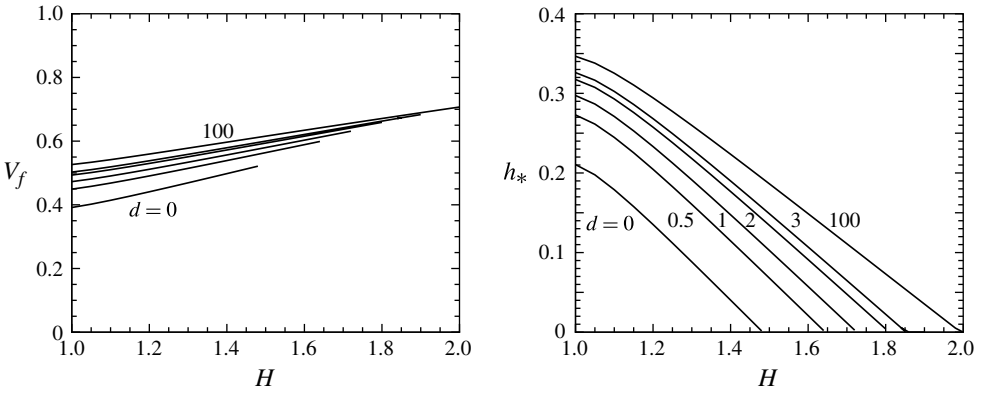


FIGURE 11. Test case C. V_f and h_* of a left-moving free jump as functions of H for various d.

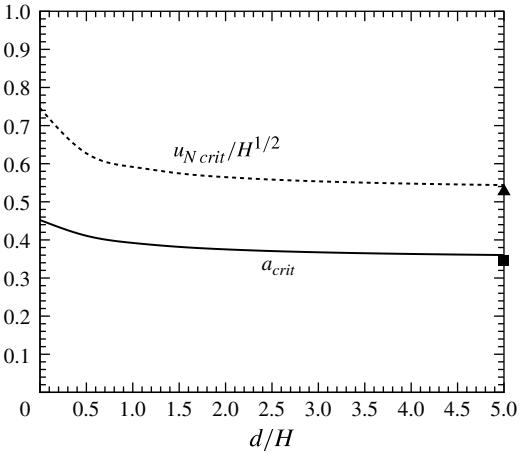


FIGURE 12. a_{crit} and $u_{Ncrit}/H^{1/2}$ as functions of $d/H = \delta$. Test case C. The symbols (square, triangle) on the right borderline show the values of a_{crit} and $u_{Ncrit}/H^{1/2}$ for the rectangular cross-section.

Consider the calculation of the critical u_N discussed in § 3.2. The condition (3.24) now reads

$$(1-\varphi)^3 = Fr_U^2 \,\frac{\delta + a}{\delta + 1/2}\, a. \tag{6.4}$$

We note that φ and Fr_U are also functions of the variable a and of the geometrical parameter δ. Therefore, for a given δ, we can obtain the value of a_{crit} beyond which the nose of the current propagates with the critical speed. The results are presented in figure 12. We observe, again, that only for $d \lesssim 2$ is the difference with the rectangular case significant.

The flow fields for trapeziums with $H = 1.2$ and various d were calculated, and the results are summarized in table 2. The case with $d = 100$ is practically a rectangle, and the case with $d = 0$ is a triangle. We see that the speed of propagation increases as d decreases, while the strength (h_*) of the left-moving jump decreases as d decreases.

https://doi.org/10.1017/jfm.2013.417 Published online by Cambridge University Press

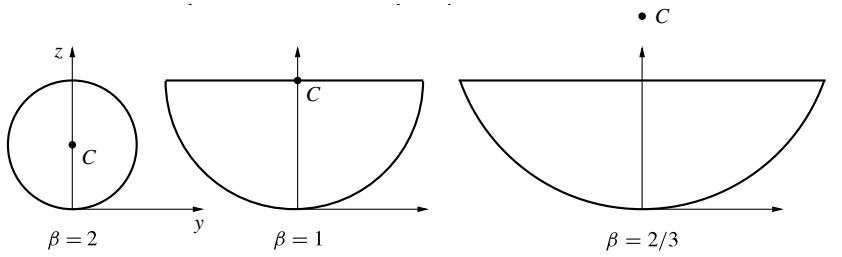


FIGURE 13. A sketch of the circle-segment cross-section for three values of the parameter β. The point C is the centre of the circle.

d	h_*	V_f	h_X	h_{core}	u_{core}	c_M	c_Q	h_N	u_N	Type
0	0.135	0.441	0.619	0.471	0.809	0.380	*	0.471	0.809	2
1	0.233	0.512	0.482	0.450	0.657	0.081	*	0.450	0.657	2
2	0.256	0.530	0.456	0.447	0.625	0.027	*	0.447	0.625	2
100	0.294	0.559	0.447	0.447	0.575	−0.055	0.531	0.418	0.579	1

TABLE 2. Flow field properties for the trapezium $f(z) = (d + z)/(d + 1)$, $H = 1.2$, as functions of d (see figure 2). The asterisk $(*)$ in c_Q column means that point Q is virtual because the nose is subcritical. h_X is the height at $x = 0$.

This is consistent with our conjecture that the expansion of the channel makes the current behave as in a deeper ambient.

7. Test case D: circle sector

Consider a circle-sector cross-section: the lower boundary is a circular tube of radius r^*, which is cut by the top plane at height H^*. The asterisks denote dimensional variables. It is convenient to introduce the dimensionless parameter

$$\beta = H^*/r^* \quad (\beta \leqslant 2). \tag{7.1}$$

The full-circle cross-section is given by $\beta = 2$, while a half-circle channel is represented by $\beta = 1$ (see figure 13).

It is convenient to scale both the z and y lengths by h_0. The cross-section function is therefore $f(z) = 2[2(H/\beta)z - z^2]^{1/2}$, $0 \leqslant z \leqslant H$. The calculations of A, A_T, φ and Fr_U can be performed by analytical formulas, which we present in appendix B. These results are then used in the subsequent stages of solution.

A backward-moving jump develops for $H < H_{crit}(\beta)$. Typical results for V_f and h_* are shown in figure 14. Interestingly, the behaviour is almost unchanged when β varies from 1 to 0.1. (This can be connected to the approximations (B 6), which apply for $\beta \leqslant 1$.) An experimental verification of this effect seems feasible.

The nose moves with critical speed for values of $a \geqslant a_{crit}$. Typical results are shown in figure 15.

We solved in detail for several combinations of β and H.

Consider first the full-circle channel $\beta = 2$. The flow field results are summarized in table 3. The full-depth lock $H = 1$ case displays a novel flow field structure, which we label Type 4. The calculations show that it is not possible to connect smoothly,

https://doi.org/10.1017/jfm.2013.417 Published online by Cambridge University Press

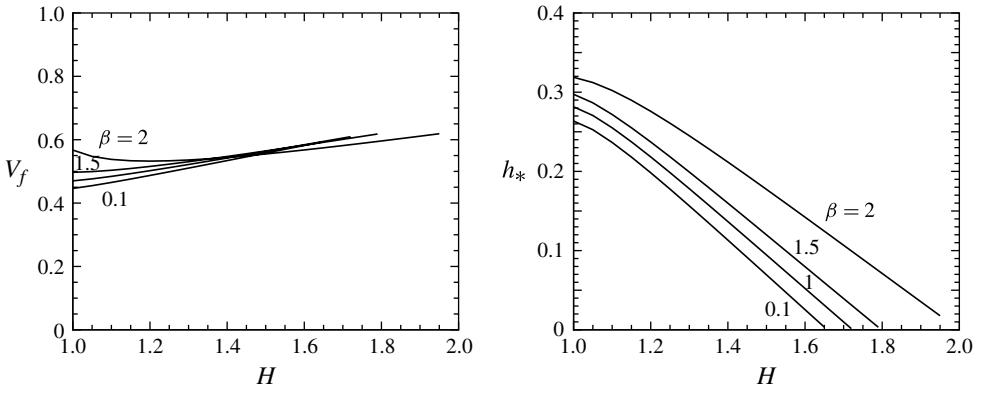


FIGURE 14. The circle case. V_f and h_* of a left-moving free jump as functions of H for $\beta = 0.1, 1, 1.5, 2$.

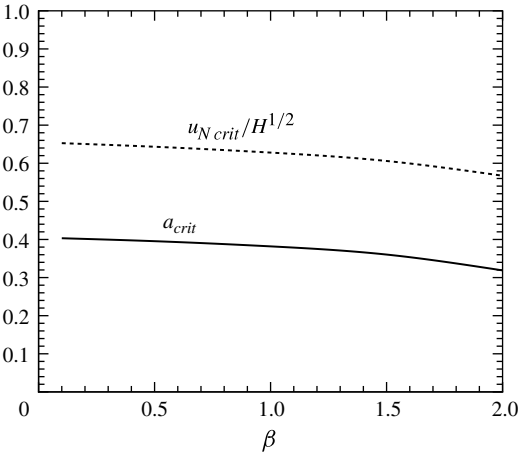


FIGURE 15. The circle case. a_{crit} and $u_{Ncrit}/H^{1/2}$ as functions of β.

using c_+ and c_- characteristics, the free back-moving jump and nose. Due to symmetry, we expect a core with $h_{core} = 1/2$. However, the integration on the c_+ characteristic, starting with the $(h_j, u_j) = (0.68117, 0.21462)$ conditions next to the jump (provided by the solution of (3.16) and (3.20)) is physically acceptable only until h reaches the value 0.522. For smaller values of h, the square roots of (3.4)–(3.5) give complex values. We first checked whether a restricted jump (with larger h_j and smaller u_j), in accord with the 'first equation' discussed in § 3.1, can resolve this difficulty. We found that this avenue takes us in the wrong direction: the mismatch becomes more pronounced. A similar difficulty appears for the integration on the c_- characteristic from the critical nose to smaller values of x: the attainable maximum is $h = 0.478$. We therefore conjecture that the expected simple core with $h = 1/2$ is unattainable, and hence the solution is closed by an internal jump. Indeed, a (quite weak) jump at $x = 0$ of height 0.044 can connect between the $h = 0.522$ domain on the left and $h = 0.478$ on the right, as sketched in figure 16. This structure is an interesting issue

https://doi.org/10.1017/jfm.2013.417 Published online by Cambridge University Press

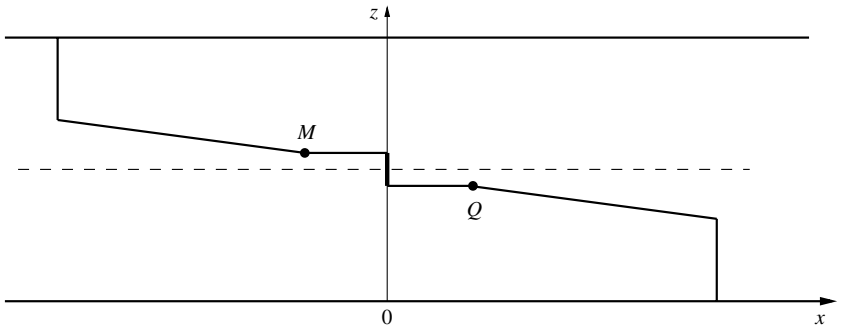


FIGURE 16. A schematic description of the Type 4 flow field in the full-circle full-depth problem, $\beta = 2$, $H = 1$. See table 3 for more details.

H	h_*	V_f	h_X	h_{core}	u_{core}	c_M	c_Q	h_N	u_N	Type
1	0.318	0.567	—	0.5 ∓ 0.022	0.444 ± 0.024	−0.052	0.052	0.319	0.567	4
1.2	0.261	0.533	0.494	0.450	0.605	0.120	0.453	0.383	0.621	3
1.5	0.177	0.555	0.502	0.435	0.693	0.181	*	0.435	0.693	2
2.0	0	(0.627)	0.518	0.423	0.762	0.243	*	0.423	0.762	1

TABLE 3. Flow field properties for the full-circle cross-section, $\beta = 2$, various H. For $H = 1$, the 'core' has a jump at $x = 0$, and the $\pm$ means to the right and left of the jump (figure 16). In Types 1 and 2, the point Q is virtual. In Type 1, (V_f) is the speed of the rarefaction wave.

H	h_*	V_f	h_X	h_{core}	u_{core}	c_M	c_Q	h_N	u_N	Type
1.0	0.270	0.470	0.531	0.477	0.593	0.148	0.355	0.382	0.628	3
1.2	0.206	0.493	0.526	0.456	0.688	0.190	*	0.456	0.688	2
2.0	0	(0.657)	0.535	0.421	0.801	0.284	*	0.421	0.801	1

TABLE 4. Flow field properties for the circle-sector cross-section, $\beta = 1$, various H.

for verification by experiments and/or Navier–Stokes computations. The Type 4 flow seems to be a rare occurrence, for H very close to 1 only. At $H = 1.05$, the flow is already of Type 3.

The full-circle geometry may pose serious challenges to experimentalists concerning the handling of the 'dam'. The $\beta = 1$ case is more convenient in this respect. Pertinent results are given in table 4.

8. Comparisons with experiments

Laboratory experiments for power-law cross-sections were performed by Monaghan *et al.* (2009) and Marino & Thomas (2011). They used systems of saltwater and freshwater, which satisfy the Boussinesq assumption; the flows were in the high-Reynolds-number regime; and the release was from full-depth-lock reservoirs, $H = 1$. Unfortunately, in these experiments the attention was focused on the propagation. The

https://doi.org/10.1017/jfm.2013.417 Published online by Cambridge University Press

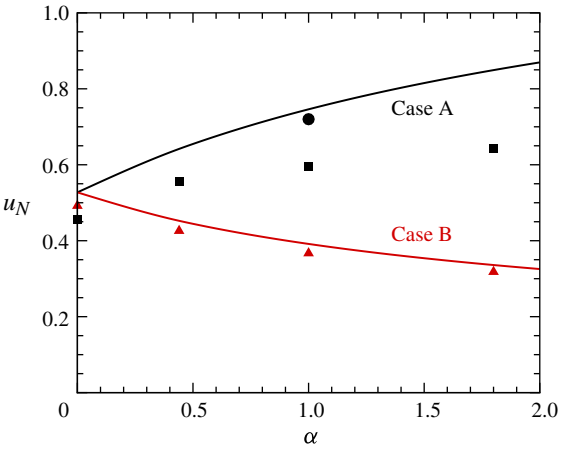


FIGURE 17. (Colour online) The speed of propagation in power-law channels, $H = 1$, for cases A and B. The lines are the SW model predictions and the symbols are experimental values (circle by Monaghan *et al.* 2009; other points by Marino & Thomas 2011).

more subtle details of the jump into the reservoir, and the critical nose, were not considered. Consequently, the only relevant comparison is for the speed of propagation. (Some data for the height of the nose of the current were also reported, but this is not a clear-cut experimental variable, and comparisons are inconclusive.)

In all the reported experiments, the speed of propagation after the dam-break was constant for a significant time interval, in accord with the SW predictions. The values of u_N are compared in figure 17, for both z^α (case A) and $(H - z)^\alpha$ (case B) channels, for various α.

We argue that, overall, the agreement is good. The qualitative trend is in full agreement. The theory predicts the experimentally observed differences between cases A (an expanding ambient) and B (a contracting ambient) well: namely, for a given α, the speed of propagation u_N in the first channel is larger than in the second one; and u_N increases with α in the first case, but decreases in the second. In all cases, the measured speed is below the theoretical value, but this is a well-known feature of inviscid SW results, because of unavoidable friction and mixing losses in the real systems. An issue of concern is the fact that in case A there is a rather large discrepancy between the theory and the data of Marino & Thomas (2011). However, for the same type of geometry, the point of Monaghan *et al.* (2009) (at $\alpha = 1$) is in quite good agreement with the prediction. The reason for this discrepancy in the experimental speed is not evident. A closer inspection reveals that the aspect ratio of the lock, $\lambda = x_0/h_0$, was $\sim$0.3 in the experiment of Marino & Thomas (2011) and $\sim$2 in the experiment of Monaghan *et al.* (2009). Therefore, the latter experiment is closer to the framework of the SW theory (which assumes a long and thin current). Bonometti, Ungarish & Balachandar (2011) point out that when $\lambda < 1$, the speed of propagation of a standard Boussinesq current is reduced below the 'long current' value, and this discrepancy becomes more pronounced when λ decreases. It makes sense to assume that a similar trend is observed here but, given the small number of data, the results are rather inconclusive.

We argue that additional experiments are necessary for a better assessment of the theory. Evidently, the discrepancy between the above-mentioned experiments must be

https://doi.org/10.1017/jfm.2013.417 Published online by Cambridge University Press

cleared up. More importantly, we argue that the speed of propagation for the reported $H = 1$ release is not a stringent test for SW models. We noticed that the corresponding u_N is a surprisingly robust theoretical result. Marino & Thomas (2009) suggested using the speed of a steady-state energy-conserving current, and Zemach & Ungarish (2013) used a one-layer model, to evaluate u_N for the reported experiments. Although there is no good *a priori* physical justification for either of these theoretical approximations for the present system, the results are within a few per cent of the more rigorous two-layer model predictions. For example, for the triangle $f(z) = z$, the steady-state energy-conserving, one-layer and two-layer calculations yield $u_N = 0.72, 0.73, 0.75$, respectively. The suggested explanation for this robustness is the critical (choked) speed of the nose-front. At this maximum, $\mathrm{d}u_N/\mathrm{d}h_N = 0$ and hence u_N are quite insensitive to variations of h_N about this point. Since the less rigorous models use the same continuity equation and Fr function as the two-layer model, they cannot deviate too much from the value of h_N, and even less that of u_N. Moreover, the rigorous two-layer calculations show that u_N is time-independent for a significant time and that the dissipation at the nose is small; consequently, the steady-state energy-conserving assumption can be justified, *a posteriori*, as a good approximation for the calculation of u_N in the considered experimental settings. It is encouraging that three different models agree concerning the value of u_N, but our claim is that in such circumstances it is not possible to lend convincing experimental support to the predictive power of the two-layer model, and to the need for such a model at all.

It will therefore be more effective, for systems with H close to 1, to examine the agreements between experiment and present theory concerning the shape of the interface; in particular, the presence/absence of jumps and rarefaction waves into the reservoir, and the reflected bore. Also, comparisons concerning the influence of H are necessary. We hope that our results will serve as a motivation and as guidelines for further experimental work on this problem.

9. Concluding remarks

We have presented a shallow-water two-layer investigation of the dam-break problem, which generates high-Reynolds-number gravity currents in a channel with non-rectangular cross-section. The sidewalls of the channel are the quite general $y = -f_1(z), y = f_2(z)$. We have shown that an efficient and consistent generalization of the standard system, developed for a rectangular cross-section (or an infinitely wide channel), is obtained. The variables are the height $h(x, t)$ of the interface (measured from the lowest line on the bottom), and the velocity $u(x, t)$ (averaged over the cross-area of the current). The continuity and momentum equations, supplemented by the Froude-number condition at the nose, are formally quite similar to the classical system. The geometry enters the formulation via the width function $f(z) = f_1(z) + f_2(z)$, and integrals of $f(z)$ and $zf(z)$. For a given geometry, the free input parameters are the height ratio of the ambient to the current in the lock, H, and the density ratio of light to heavy fluids, R. The formulation is self-contained and does not use any adjustable constants.

We have shown that the problem is amenable to dam-break solutions by the method of characteristics. The geometry of the cross-section imposes various restrictions on the return flow in the ambient, and hence on the propagation of disturbances by the characteristics. Consequently, jumps (shocks) and other 'critical' conditions may develop. We have formulated the appropriate jump conditions and restrictions, taking into account the contribution of $f(z)$. We have also presented a brief description of the

https://doi.org/10.1017/jfm.2013.417 Published online by Cambridge University Press

reflected bore. To our knowledge, this analysis is novel. The formulations given in this study are for both Boussinesq and non-Boussinesq systems, but detailed solutions are given only for Boussinesq systems ($R = 1^-$).

We have presented detailed solutions for typical geometries: power-law $f(z) = z^\alpha$, trapezoidal and circle (full and sector). We have focused our attention on the fundamental full-depth 'lock-exchange' configuration ($H = 1$), and also on part-depth lock-release $H > 1$ cases. In all the tested cases, the theory seems to work well, and the results seem physically acceptable. The two-layer analysis is most relevant when there is a significant return flow in the ambient adjacent to the current. Qualitatively, the effect of the return flow in the ambient is (in almost all tested cases) as in the rectangular case: when H is close to 1, the motion into the reservoir propagates as a jump (rather than as a rarefaction wave) and the speed of the nose is restricted (critical) by the speed of the characteristic. A novel feature, unexpected in the rectangular geometry, was noticed for the full-circle geometry: a (quite weak) internal jump appears in the core where the interface is horizontal. In general, as H increases, the influence of the return flow decays, the interface between the reservoir and the nose becomes smoother, and the one-layer-model pattern of flow (Type 1) is recovered. The details depend strongly on the width function $f(z)$.

The predicted behaviour of the speed of propagation is in fair agreement with the available experiments. However, the available experiments were not concerned with the details of the jumps and critical conditions of propagation that are highlighted by the present solution. Therefore, there are no corroborations of the components of the flow field. These details require a dedicated experimental investigation, which we hope will be motivated by this paper. We note that the tested geometries were symmetric with respect to $y = 0$. Consequently, the (inviscid) solution remains valid in a half-channel obtained by a vertical wall at midplane $y = 0$. This observation may be useful for the design of experimental devices.

The present analysis is a very significant generalization of the classical two-layer gravity–current dam-break problem. We now have insights into the effect of the cross-section geometry, and a predictive tool for the flow-field values in a given configuration. The classical rectangular (or laterally unbounded) channel is now just a particular case, $f(z) = \text{const.}$, in the wide domain of cross-sections covered by the new model. Since the formulation is valid for any $0 < R < 1$, we think that this paper provides a convenient base for extending the reported solutions into the non-Boussinesq domain. The combination of non-rectangular cross-section geometry with non-Boussinesq effects is an interesting topic, the investigation of which (by analytical, numerical and experimental means) in open to future research.

The dam-break solution predicts only the initial phase of propagation of the gravity current. In a channel significantly longer than the reservoir, the nose is expected to propagate with the dam-break u_N until the reflected bore (or rarefaction wave) from the backwall catches up with the nose. Our analysis of the characteristics indicates that this so-called 'slumping' phase will indeed be present in the non-rectangular channel. The details of the flow beyond the dam-break solution, for a general $f(z)$, require a numerical solution (typically by finite differences) of the equations of motion. The present analytical solutions provide useful guidelines and test cases for such a code. However, the production of reliable numerical results is a non-trivial task in view of the jumps, critical speeds and bore that may appear in the two-layer solution. This topic is left for future work.

https://doi.org/10.1017/jfm.2013.417 Published online by Cambridge University Press

Acknowledgements

The author wishes to thank Professor L. Thomas for providing the data for figure 17, and Dr T. Zemach for useful comments.

Appendix A. Left-moving jump details

The evaluations of the speed and dissipation of the jump into the reservoir can be reduced to straightforward calculations as follows.

We substitute the continuity relationships (3.10) into the flow-force result (3.15). We divide by $\rho_c A_T$, and scale the variables according to (2.15).

Here, we assume that $h_1 = 1 - h_*$ is given. (This resembles the use of Benjamin's analysis for a given height of the current.)

Recall that

$$A_T = \int_0^H f(z)\,\mathrm{d}z; \quad \varphi_0 = \left(\int_0^1 f(z)\,\mathrm{d}z\right) \Big/ A_T; \quad \varphi_1 = \left(\int_0^{h_1} f(z)\,\mathrm{d}z\right) \Big/ A_T. \quad \text{(A 1)}$$

Here, we use dimensionless variables (unless stated otherwise).

Let

$$K_1 = \varphi_0/\varphi_1; \quad K_2 = (1-\varphi_0)/(1-\varphi_1) \quad \text{(A 2)}$$

$$s = -\varphi_0(1-K_1) - R(1-\varphi_0)(1-K_2) + \frac{1}{2}\frac{\rho_S}{\rho_c}\left(1-K_2^2\right) \quad \text{(A 3)}$$

$$q = \varphi_0 - h_1\varphi_1 - \frac{1}{A_T}\int_{h_1}^1 z f(z)\,\mathrm{d}z \quad \text{(A 4)}$$

(note that $K_i = u_i'/V_f$). We obtain

$$V_f^2 = q/s. \quad \text{(A 5)}$$

After some algebra, we can cast s in a more explicit form:

$$s = (\varphi_0 - \varphi_1)\left[\frac{\varphi_0}{\varphi_1} - R\frac{1-\varphi_0}{1-\varphi_1} + \frac{1}{2}\frac{\rho_S}{\rho_c}\frac{2-\varphi_0-\varphi_1}{(1-\varphi_1)^2}\right]. \quad \text{(A 6)}$$

Recall that ρ_S is ρ_a when $H > 1$, and ρ_c when $H = 1$. In the Boussinesq case, $R = 1$ and $\rho_S/\rho_c = 1$, which allows a further simplification of the expressions given above.

We wish to emphasize that (A 5) is a general and fundamental result, which covers a wide range of two-layer systems: Boussinesq and non-Boussinesq, in rectangular and non-rectangular cross-section geometry. (Actually, Benjamin's result, and the extension (2.13), are both recovered when the fluid on the left fills the channel. The interpretation is that the jump is the front of the light current propagating to the left.)

The energy dissipation is calculated from (3.22) by similar substitutions. Let

$$Q = -\frac{1}{2}V_f^3\left[\varphi_0(1-K_1^2) + R(1-\varphi_0)(1-K_2^2) - \frac{\rho_S}{\rho_c}\left(1-K_2^2\right)\right] - \varphi_0 V_f(1-h_1). \quad \text{(A 7)}$$

It can be verified that this is the dimensional rate of dissipation divided by $A_T\rho_c U^3$. Therefore, $2Q/\varphi_0$ gives the properly scaled $\dot{\mathscr{D}}$. The computation of this variable, after the calculation of V_f, is straightforward. A more explicit expression can be obtained upon the substitution of (A 2) and (A 5).

We recall that, when $H > 1$, we used Bernoulli's equation across the jump for the upper, expanding, layer; this implies energy conservation in this layer. The dissipation

https://doi.org/10.1017/jfm.2013.417 Published online by Cambridge University Press

occurs in the other layer, which contracts. In this case, we can rewrite (A 7) as:

$$Q = -\varphi_0 V_f \left(\tfrac{1}{2}V_f^2\left[1 - K_1^2 - R(1-K_2^2)\right] + 1 - h_1\right) \quad (H > 1). \tag{A 8}$$

When $H = 1$, dissipation also occurs in the contracting layer (in this case, the upper layer is co-moving with the jump).

Appendix B. Some details of the circle cross-section analysis

Consider the half-width function $\tilde{f}(z) = (2rz - z^2)^{1/2}$, for $0 \leqslant z \leqslant h$ $(\leqslant 2r)$. The necessary integrals are

$$I(h) = \int_0^h (2rz - z^2)^{1/2}\,\mathrm{d}z = \frac{1}{2}\left[(h-r)(2rh-h^2)^{1/2} - r^2\arcsin(1-h/r) + r^2\frac{\pi}{2}\right]; \tag{B 1}$$

$$J(h) = \int_0^h (2rz - z^2)^{1/2} z\,\mathrm{d}z = -\frac{1}{3}(2rh-h^2)^{3/2} + rI(h). \tag{B 2}$$

Let $r = H/\beta$, see figure 13. We find that $A = 2I(h)$, $A_T = 2I(H)$, and hence

$$\varphi = I(h)/I(H). \tag{B 3}$$

The use of (2.13) yields

$$Fr_U^2 = \frac{2(1-\varphi)}{1+\varphi}(1 - \varphi + Q), \tag{B 4}$$

where

$$Q = \frac{J(h)}{hI(H)}. \tag{B 5}$$

It can be shown that, for a given β, Fr is a function of $a = h/H$. The typical behaviour is displayed in figure 18. Recall that $\beta = 2$ means that the channel is a full circle (of radius $H^*/2$), while smaller values of β mean circular sections of radius H^*/β (the asterisks denote dimensional variables). For a larger than the values shown in the lines of the figure, the solution of Fr is energetically unacceptable.

Figure 18 indicates that $Fr(a)$ is quite insensitive to the value of β for $\beta \leqslant 1$. To understand this unexpected behaviour, we use the expansion $(2rz - z^2)^{1/2} = (2rz)^{1/2}(1 - z/(4r) + \cdots)$ in the integrands of (B 1)–(B 2). We integrate term by term, and substitute $r = H/\beta$. With an expansion for small β, we find that the leading terms are

$$\varphi = a^{3/2}; \quad Q = \tfrac{3}{5}a^{3/2}; \tag{B 6}$$

and

$$Fr_U^2 = \frac{2(1-a^{3/2})}{1+a^{3/2}}\left(1 - \frac{2}{5}a^{3/2}\right). \tag{B 7}$$

We see that β cancels out from these first-order approximate expressions. The relative error due to the neglected terms is smaller than 0.15β for φ in (B 6), and $\sim 0.25a^{3/2}\beta$ for Fr in (B 7). The approximation (B 7) is indeed in very good agreement with the exact calculation of Fr for $\beta \leqslant 1$: in figure 18, the exact line for $\beta = 0.1$ cannot be distinguished from one obtained with (B 7).

We note in passing that for a full-circle channel, the Fr_U calculations show that the current is restricted energetically to 0.437 of the height (i.e. the diameter), and the

https://doi.org/10.1017/jfm.2013.417 Published online by Cambridge University Press

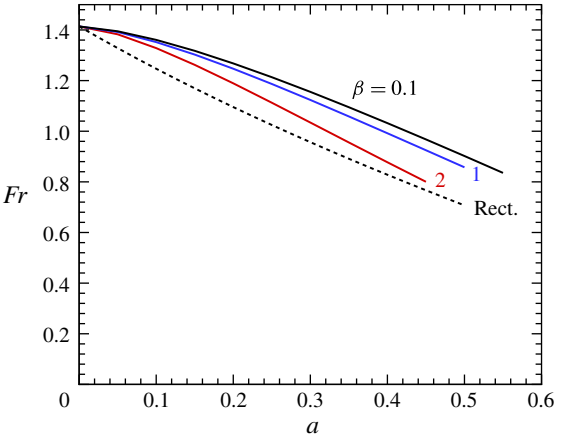


FIGURE 18. (Colour online) Fr as a function of $a = h/H$ for various β, circle $f(z) = \left[2(H/\beta)z - z^2\right]^{1/2}$. The dashed line is for the rectangular cross-section. Only values with acceptable physical dissipation are shown.

value of Fr at this point is 0.820. This upper limit of $a = h/H$ corresponds to zero dissipation. This result is in perfect agreement with the energy-conserving solution for the current in a tube presented in § 3 of Benjamin (1968).

Appendix C. The reflected bore

In flows of Types 2 and 3 (figure 2), the left-moving jump reaches the backwall $x = -1$ at time $t_f = 1/V_f$, and is then reflected with speed V_b. The behaviour in the classical rectangular case has been studied experimentally and theoretically (see Rottman & Simpson 1983 and Ungarish 2009 § 5.4.2). We expect a similar effect in the non-rectangular case, and here we derive some details.

We recall that the left-moving jump activates the fluid on the right to the conditions: the height of the interface is h_1, and the velocities in the current and ambient are $u_1 > 0$ and $u_2 < 0$, respectively. We argue that at t_f, the 'activated' ambient above the current hits the backwall with a significant speed, $|u_2|$. The wall stops this fluid abruptly, and hence the (reduced) pressure increases from zero to Π_L, and the height of the interface is pushed down from h_1 to h_{1L}. The reflected jump thus has the conditions h_1, u_1, u_2 on the right and $h_{1L}, 0, 0$ on the left (see figure 19).

To calculate the jump height $h_{**} = h_1 - h_{1L}$ and speed V_b, we use a system attached to the bore and moving with speed V_b (to the right). The velocities u_i in the laboratory system are transformed to $u_i' = u_i - V_b$. The additional subscript L is used to denote the variables in the left domain, between the wall and the reflected bore. Note that

$$u_{1L}' = u_{2L}' = -V_b. \tag{C 1}$$

Continuity of volume fluxes gives

$$u_{1L}' A_{1L} = u_1' A_1 \quad \text{and} \quad u_{2L}'(A_T - A_{1L}) = u_2'(A_T - A_1). \tag{C 2}$$

Combining (C 1)–(C 2) yields

$$V_b = u_1 \frac{A_1}{A_1 - A_{1L}} = u_1 \frac{\varphi_1}{\varphi_1 - \varphi_{1L}}. \tag{C 3}$$

https://doi.org/10.1017/jfm.2013.417 Published online by Cambridge University Press

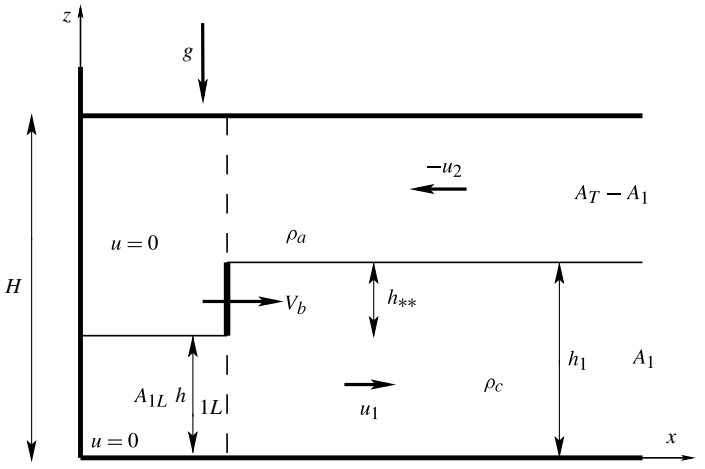


FIGURE 19. A schematic description (in the laboratory frame) of the flow near the endwall, shortly after the formation of the reflected bore. The speed of the bore is V_b, and the depression of the interface due to the impingement of the ambient flow on the wall is h_{**}.

The φ variable is, again, the area ratio of the current to the total for the channel, A_T,

$$\varphi_{1j} = \left(\int_0^{h_{1j}} f(z)\,\mathrm{d}z \right) \Big/ A_T, \tag{C 4}$$

where $j = L$ or blank.

We recall that u_1 and h_1 (and, hence, also A_1 and φ_1) are known from the dam-break solution. To determine V_b, we need only one additional value, h_{1L}. To this end, we apply the momentum balances. The hydrostatic pressures, supplemented by Bernoulli's equation on the streamline $z = H$, for the right and left sides of the jump, read (dimensional)

$$\Pi_r = \begin{cases} \mathscr{C} + \Delta\rho g(h_1 - z) & (\text{over } A_1) \\ \mathscr{C} & (\text{over } A_T - A_1); \end{cases} \tag{C 5}$$

$$\Pi_L = \begin{cases} \mathscr{C} + \frac{1}{2}\rho_a \left(u_2'^2 - V_b^2\right) + \Delta\rho g(h_{1L} - z) & (\text{over } A_{1L}) \\ \mathscr{C} + \frac{1}{2}\rho_a \left(u_2'^2 - V_b^2\right) & (\text{over } A_T - A_{1L}). \end{cases} \tag{C 6}$$

The x-momentum balance for a control volume about the jump is

$$\rho_c u_1' A_1 (u_1' - u_{1L}') + \rho_a u_2' (A_T - A_1)(u_2' - u_{2L}') = \iint_{A_T} \Pi_L\,\mathrm{d}A - \iint_{A_T} \Pi_r\,\mathrm{d}A. \tag{C 7}$$

The left-hand side is the rate of change of momentum (outflux minus influx), and this is balanced by the pressure forces, expressed by the right-hand side. To simplify this equation, we substitute the above results for the pressure, express all velocities as multiples of V_b, employ the continuity relationships, scale the variables and

https://doi.org/10.1017/jfm.2013.417 Published online by Cambridge University Press

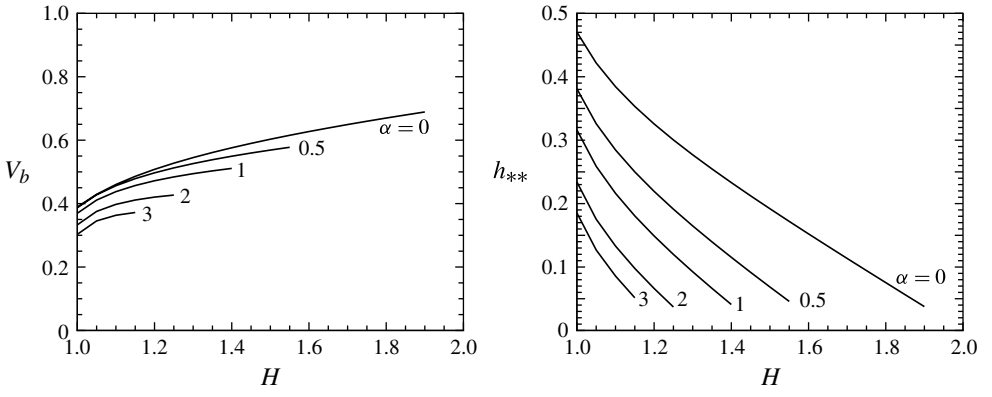


FIGURE 20. V_b and $h_{**} = h_1 - h_{1L}$ of a reflected jump as functions of H for various α, $f(z) = z^\alpha$, in a Boussinesq system.

divide (C 7) by A_T. The result (dimensionless) is

$$\left[u_1 \frac{\varphi_1}{\varphi_1 - \varphi_{1L}}\right]^2 \left[\varphi_{1L}(K_1 + 1) + R(1 - \varphi_{1L})(K_2 + 1) - \frac{1}{2}R(K_2^2 - 1)\right]$$
$$= h_{1L}\varphi_{1L} - h_1\varphi_1 + \left(\int_{h_{1L}}^{h_1} zf(z)\,\mathrm{d}z\right) \Big/ A_T, \tag{C 8}$$

where $R = \rho_a/\rho_c$, and

$$K_1 = -\varphi_{1L}/\varphi_1; \quad K_2 = -(1 - \varphi_{1L})/(1 - \varphi_1). \tag{C 9}$$

This is a general result for the reflected jump (bore) in a channel of cross-section shape $f(z)$, for both Boussinesq and non-Boussinesq systems. The numerical calculation of h_{1L} from (C 9) is straightforward (we used a secant-method iteration); then V_b is calculated using (C 3).

Results for the power-law geometry are illustrated in figure 20. We see that the strength of the reflected bore decreases when H and α increase. This is a straightforward consequence of the observation that the effect of the left-moving jump decreases in the same circumstances. In all the tested cases, we found that $V_b/V_f < 1$, which was to be expected. (In the rarefaction-wave limit, $V_b/V_f = 1$.)

The speed of the reflected bore is expected to increase during the propagation, because the thickness of the current decreases with x. It is therefore not straightforward to calculate analytically when the reflected bore will reach the nose of the current (which propagates with the constant u_N until this intersection occurs). However, we can estimate the trend. The results of figure 20 for the power-law cross-section indicate that, for a fixed α, V_b increases with H; therefore, the slumping time interval is expected to decrease with H. The similar trend is known to occur in the rectangular cross-section. For a fixed H, when α increases, u_N increases and V_b decreases. This suggests that the slumping time (and distance) increase with α.

When the dam-break flow is of Type 1, the speed of the rarefaction wave into the reservoir is given by c_-, with $h = 1, u = 0$. When this reaches the endwall, it is reflected with the same speed in the opposite direction, c_+. Using (3.5), the

https://doi.org/10.1017/jfm.2013.417 Published online by Cambridge University Press

corresponding dimensionless velocities are

$$c_{\pm} = \pm\sqrt{\frac{1-\varphi_0}{1-(1-R)\varphi_0}A_0} \tag{C 10}$$

where the subscript 0 means the initial reservoir, $h = 1$.

It is expected that numerical solutions (in particular, the finite difference method used in Zemach & Ungarish 2013) of the hyperbolic system (3.2) will provide the details of the flow after the reflection of the jump (or wave) efficiently. This investigation is left for future work.

REFERENCES

Benjamin, T. B. 1968 Gravity currents and related phenomena. *J. Fluid Mech.* **31**, 209–248.

Bonometti, T., Ungarish, M. & Balachandar, S. 2011 A numerical investigation of constant-volume non-Boussinesq gravity currents in deep ambient. *J. Fluid Mech.* **673**, 574–602.

Borden, Z., Meiburg, E. & Constantinescu, G. 2012 Internal bores: an improved model via a detailed analysis of the energy budget. *J. Fluid Mech.* **703**, 279–314.

Klemp, J. B., Rotunno, R. & Skamarock, W. C. 1994 On the dynamics of gravity currents in a channel. *J. Fluid Mech.* **269**, 169–198.

Klemp, J. B., Rotunno, R. & Skamarock, W. C. 1997 On the propagation of internal bores. *J. Fluid Mech.* **331**, 81–106.

Lowe, R. J., Rottman, J. W. & Linden, P. F. 2005 The non-Boussinesq lock exchange problem. Part 1. Theory and experiments. *J. Fluid Mech.* **537**, 101–124.

Marino, B. M. & Thomas, L. P. 2009 Front condition for gravity currents in channels of nonrectangular symmetric cross-section shapes. *Trans. ASME J. Fluids Engng* **131** (5), 051201.

Marino, B. M. & Thomas, L. P. 2011 Dam-break release of a gravity current in a power-law channel section. *J. Phys.: Conference Series* **296**, 012008 doi:10.1088/1742-6596/296/1/012008.

Monaghan, J., Mériaux, C., Huppert, H. & Monaghan, J. 2009 High Reynolds number gravity currents along V-shaped valleys. *Eur. J. Mech.* – B/*Fluids* **28** (5), 651–659.

Rottman, J. & Simpson, J. 1983 Gravity currents produced by instantaneous release of a heavy fluid in a rectangular channel. *J. Fluid Mech.* **135**, 95–110.

Rotunno, R., Klemp, J. B., Bryan, G. H. & Muraki, D. J. 2011 Models of non-Boussinesq lock-exchange flow. *J. Fluid Mech.* **675**, 1–26.

Simpson, J. E. 1997 *Gravity Currents in the Environment and the Laboratory*. Cambridge University Press.

Ungarish, M. 2009 *An Introduction to Gravity Currents and Intrusions*. Chapman & Hall/CRC Press.

Ungarish, M. 2010 Energy balances for gravity currents with a jump at the interface produced by lock release. *Acta Mech.* **211**, 1–22.

Ungarish, M. 2011 Two-layer shallow-water dam-break solutions for non-Boussinesq gravity currents in a wide range of fractional depth. *J. Fluid Mech.* **675**, 27–59.

Ungarish, M. 2012 A general solution of Benjamin-type gravity current in a channel of non-rectangular cross-section. *Environ. Fluid Mech.* **12** (3), 251–263.

Zemach, T. & Ungarish, M. 2013 Gravity currents in non-rectangular cross-section channels: analytical and numerical solutions of the one-layer shallow-water model for high-Reynolds-number propagation. *Phys. Fluids* **25**, 026601–1–24.

https://doi.org/10.1017/jfm.2013.417 Published online by Cambridge University Press